



**Ball Aerospace  
& Technologies Corp.**



JPL Document D-73509

# **TECHNOLOGY DEVELOPMENT FOR EXOPLANET MISSIONS**

## **Technology Milestone Report**

### **Advanced Speckle Sensing for Internal Coronagraphs**

**Stuart Shaklan (Co-I), Brian Kern, Amir Give'on, Kent Wallace**  
**Jet Propulsion Laboratory**

for

**Stephen E. Kendrick, PI**  
**Ball Aerospace & Technologies Corp., Boulder CO**

Charley Noecker, (Co-I), Jet Propulsion Laboratory

Jeremy Kasdin, (Co-I), Princeton University

Ruslan Belikov (Co-I), NASA Ames Research Center

**26 March 2012**

National Aeronautics and Space Administration  
Jet Propulsion Laboratory  
California Institute of Technology  
Pasadena, California

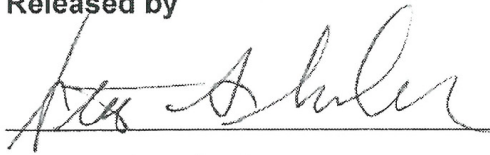
© 2012. All rights reserved.

Reference herein to any specific commercial product, process, or service by trade name, trademark, manufacturer, or otherwise, does not constitute or imply its endorsement by the United States Government or the Jet Propulsion Laboratory, California Institute of Technology.

Technology Milestone Whitepaper  
Advanced Speckle Sensing for Internal Coronagraphs – Shaklan

**APPROVALS**

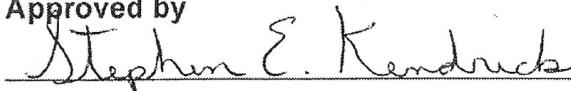
Released by

 5/11/12

Stuart Shaklan (Co-I)

Jet Propulsion Laboratory, California Institute of Technology

Approved by

 5/10/12

Stephen E. Kendrick (PI)

Ball Aerospace & Technologies Corp.

 5/11/12

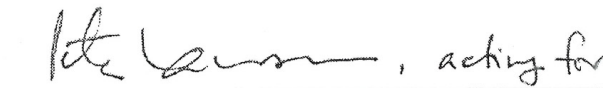
Peter R. Lawson

Exoplanet Exploration Program Chief Technologist, JPL

 5/11/12

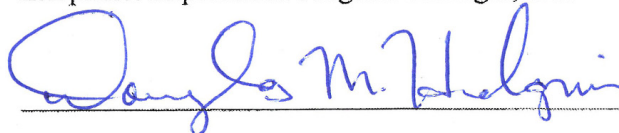
Marie Levine

Exoplanet Exploration Program Technology Manager, JPL

 , acting for 5/14/12

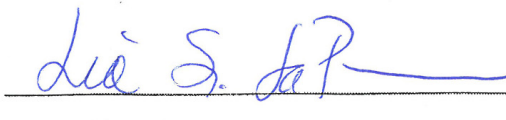
Michael Devirian

Exoplanet Exploration Program Manager, JPL

 5/15/12

Douglas Hudgins

Exoplanet Exploration Program Scientist, NASA HQ

 5/15/12

Lia LaPiana

Exoplanet Exploration Program Executive, NASA HQ

## Table of Contents

List of Acronyms .....	6
1. ABSTRACT .....	7
2. INTRODUCTION.....	7
3. EXPERIMENT OVERVIEW .....	8
3.1. <i>Pinhole Estimation Technique</i> .....	8
3.2. <i>HCIT Configuration: Changes Since TPF-C Milestone #2</i> .....	11
3.3. <i>Broad Band Spectrum</i> .....	12
4. MILESTONE PROCEDURES .....	13
4.1. <i>Definitions</i> .....	14
4.1.1. “Raw” Image and “Calibrated” Image.....	14
4.1.2. Starting from scratch.....	14
4.1.3. Testbed “star” source .....	14
4.1.4. Contrast map.....	14
4.1.5. Speckle field map.....	15
4.1.6. Dark hole .....	15
4.1.7. Contrast value .....	15
4.1.8. Control algorithm.....	15
4.1.9. Phase Diversity CSD measurement .....	15
4.1.10. Pinhole CSD measurement .....	15
4.1.11. Statistical Confidence .....	16
4.2. <i>Photometric Normalization</i> .....	17
4.3. <i>Success Criteria</i> .....	20
4.3.1. Light source .....	20
4.3.2. Contrast performance.....	21
4.3.3. Incoherent stray light background.....	21
4.3.4. Duration and robustness.....	22
4.3.5. Certification Process .....	22
4.3.6. Milestone Certification Data Package.....	23

Technology Milestone Whitepaper  
Advanced Speckle Sensing for Internal Coronagraphs – Shaklan

5.	NARRATIVE REPORT.....	25
5.1.	<i>Data Acquisition</i> .....	25
5.2.	<i>Low-Pass Filtering of Image Plane Data</i> .....	29
5.3.	<i>Results</i> .....	30
5.4.	<i>Statistical Confidence</i> .....	31
6.	CONCLUSION .....	32
7.	REFERENCES.....	34
	<b>APPENDIX I. PINHOLE BASED ESTIMATION</b> .....	35
	<b>APPENDIX II. THERMAL DATA</b> .....	36
	<b>APPENDIX III. ESTIMATED CONTRAST AND PHASE</b> .....	37

## **List of Acronyms**

**ASSIC – Advanced Speckle Sensing for Internal Coronagraphs**

**CCD – Charge Coupled Device**

**CSD – Coherent Speckle detection**

**DM – Deformable Mirror**

**EFC – Electric Field Conjugation wavefront control algorithm**

**FWHM – Full Width at Half Maximum**

**HCIT – High Contrast Imaging Testbed**

**OAP – Off-axis parabola**

**PD – Phase Diversity**

**PH – Pinhole Diversity**

**PSF – Point Spread Function**

**SM – Single Mode**

**TDEM – Technology Development for Exoplanet Missions**

**TPF-C – Terrestrial Planet Finder Coronagraph**

## 1. ABSTRACT

This report discusses the completion of the Advanced Speckle Sensing for Internal Coronagraphs (ASSIC) proposal, funded under the 2009 Technology Development for Exoplanet Missions initiative. ASSIC was a laboratory verification of consistency of dark-hole contrast estimation in a band-limited coronagraph to better than  $2 \times 10^{-9}$  using two independent estimation approaches: deformable mirror phase diversity, and reference beams formed using pinholes adjacent to the Lyot stop. This was achieved in broad band light having a 10% fractional bandwidth over a region  $5 \times 18 \lambda/D$  wide. Statistically we achieved  $> 99.5\%$  confidence that our measurements met the milestone requirements.

Here we report on changes to the High Contrast Imaging Testbed (HCIT) since the completion of TPF-C milestone #2 in 2008<sup>1</sup>, the pinhole configuration and approach, the laboratory procedures and data, and the statistical verification that the milestone has been met.

## 2. INTRODUCTION

The completion of TPF-C Milestone #2 proved that it is possible to estimate the complex field in the image plane and to control scattered light to levels better than  $10^{-9}$ , in broadband light, over a region several  $\lambda/D$  wide.<sup>1</sup> The estimation technique was based on phase diversity (PD) generated with patterns commanded on the Deformable Mirror (DM). In theory, as long as one has a means of accurately estimating the contrast, then with enough degrees of freedom and adequate calibration of the DM, the contrast can be controlled to arbitrarily deep levels. But in reality, for a number of reasons (e.g., number of degrees of freedom, stability) the convergence bottoms out and speckles remain at levels that can mask the presence of a planet.

Several approaches may allow the speckles to be identified and subtracted from the image in space applications. Roll subtraction is the differencing of images made at two or more roll angles about the line-of-sight. If the telescope remains stable during the roll, the speckles remain static on the detector while the planet moves according to the roll angle.<sup>2</sup> The challenges here are twofold: first, the time to record two images is longer than the time to record a single image, so the overall stability time frame grows. Second, the telescope and instrument are subject to different solar illumination and this drives the wavefront to change; even picometer level changes are enough to distort the speckles and mask the presence of an earth-like planet.

Another approach is spectral deconvolution, in which one tries to take advantage of the natural linear spectral scaling of the speckles with wavelength.<sup>3</sup> While this may be effective at large working angles and wide bandwidth, the situation encountered in space-based coronagraphy with a large telescope (e.g. 8 m diameter) is that the working angles are small (e.g.  $\leq 4 \lambda/D$ ), and the practical bandwidths are relatively narrow (10-20%). Under these conditions, there is little spectral evolution of the speckles and they remain difficult to distinguish from a planet. Further, the wavefront control system removes the low-order wavelength-dependent light, leaving high-order terms with different wavelength-dependence from speckle to speckle. We have found that spectral deconvolution in these conditions is effective if the location of the planet is known.<sup>4</sup>

The purpose of the Advanced Speckle Sensing for Internal Coronagraphs (ASSIC) TDEM is to develop an independent means of estimating the complex electric field to confirm the accuracy of the phase

diversity estimation. We developed an interferometric approach that is a variant of the self-coherent camera introduced by Baudoz.<sup>5,6,7</sup> We place pinholes just outside the edge of the Lyot stop, in the region where the diffracted light is blocked. The pinholes (PH) are opened one or two at a time to generate tilted wavefronts in the image plane. These wavefronts serve as reference beams that interfere with the light that passes through the center of the Lyot stop. A mathematical treatment similar to that of PD provides an estimate of the complex field in the image. The main difference between PH and PD estimation is that with PD we difference pairs of images that introduce opposing changes in the image plane, whereas with PH we difference each diversity image with the non-diversity image.

There are two important advantages to the PH approach. First, except for a sliding mask that blocks and unblocks the pinholes, there are no moving parts. Whereas PD requires moving the hysteretic, non-linear DM, the PH approach simply requires exposing the image plane to light that passes through the pinholes. Second, the additive electric field from the pinholes can be treated without approximation in the image plane. This is not the case for PD, which modifies the phase of the field in the pupil but does not exactly add field ( $e^i$  is treated as  $1+i\varphi$ ). This can be a limiting factor because our wavefront control technique (Electric Field Conjugation, or EFC<sup>8</sup>) does not flatten the phase in the pupil, it finds the phase that removes light from the dark hole region. Thus  $\varphi$  is not necessarily small.

Originally implemented in the ASSIC TDEM as a technique for reducing the speckle estimation time in the presence of exozodiacal or other incoherent light, this attribute of the pinhole approach is shared with phase diversity. It is not clear that either approach has an intrinsic advantage as the coherent ‘boost’ from the diversity or reference beam grows. With PD, diversity in the image plane modulation is increased when the DM stroke is increased, but this adds non-linearity and hysteresis that may be difficult to calibrate. With pinholes, the reference beam field is increased by expanding the pinhole diameter, but this introduces chromatic illumination gradients across the pinhole. Per the ASSIC TDEM White Paper,<sup>9</sup> the goal of our TDEM work was to compare PD and PH performance at specific contrast level ( $10^{-8}$ ). We have not attempted to show how either approach reduces the sensing time, and we have not compared in detail the calibration issues at different contrast levels, though this is a subject of great interest.

### **Milestone Statement**

*Using coherent speckle detection methods, demonstrate the capability to measure speckles of  $1 \times 10^{-8}$  contrast with uncertainty, stability, and repeatability of 20% in intensity and 1 radian in phase with 90% statistical confidence, in a window at least  $2 \times 2 \lambda_0/D$  wide at  $< 10 \lambda_0/D$  from the star, in one spectral band of width  $> 10\%$ , with a uniform incoherent background of at least  $1 \times 10^{-8}$  in the area covered by the PSF.*

## **3. EXPERIMENT OVERVIEW**

### **3.1. Pinhole Estimation Technique**

The experiment approach was first described by Noecker *et al.*<sup>10</sup> In a band-limited Lyot coronagraph configuration, we place four pinholes in locations that allow reasonably robust solutions for the speckle field with a good distribution of phases at each pixel. (fig. 1). We have designed and implemented a shutter mechanism for selecting which pinholes are open to illuminate the focal plane.

- With all pinholes blocked and the main opening of the Lyot stop unblocked, we can take science data, and calibrate the speckle intensity with no reference beams. This state is also used for DM Phase Diversity.
- Using each pinhole unblocked one at a time with the main opening of the Lyot stop unblocked, we can capture interference images to support a solution for the speckle fields.
- Using all combinations of two pinholes unblocked with the main opening of the Lyot stop blocked, we can also cross-calibrate the reference fields themselves, validating the reference field amplitude and phase estimates and improving the speckle solution.

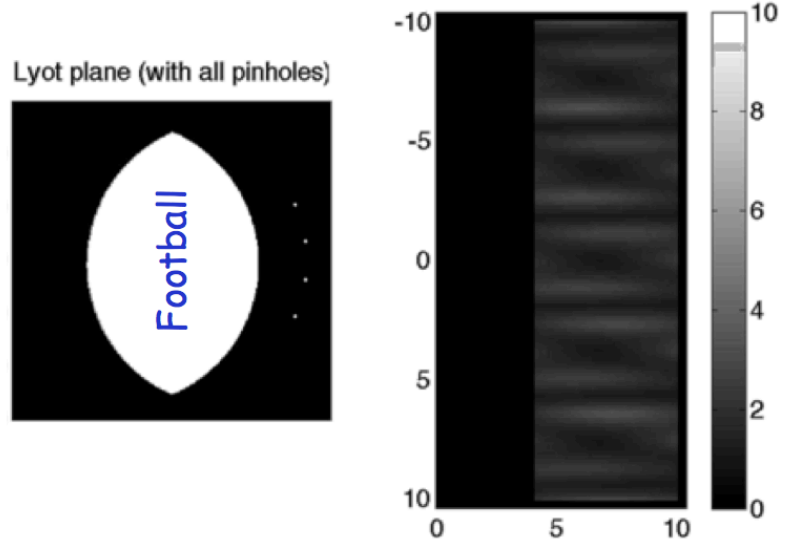


Figure 1. Pinholes adjacent to the Lyot stop, and quality of solution. Left: Arrangement of pinholes around the outside of the central opening of the Lyot stop. The “Football” is the traditional opening of the Lyot mask, where the planet light and speckles pass through the Lyot stop. This one is tailored for a linear band-limited mask and as  $\epsilon=0.34$ . The edge radius of curvature is 24 mm. The four pinholes are arranged on an arc at right. Right: the condition number at each pixel for a best solution for PH diversity-derived speckle fields. XY axes are equivalent sky angles in units of  $\lambda/D$ . Within the range from 4–10  $\lambda/D$ , the minimum condition number is 1 (ideal, and the maximum is 3.17).

With our PH-derived estimate of the speckle fields, we may choose to correct the speckles using the DM or simply to estimate and subtract the speckle intensity from the science data.

Figure 1 shows the arrangement of pinholes around the outside of the Lyot stop opening, and the condition number for the optimal solution for speckle fields. Solving for the real and imaginary parts of  $E_0$  involves inversion of the matrix in equation A1 (Appendix I) for each of the pixels in the region of interest (each pixel has a unique matrix to invert). In the current configuration, the matrix is over-determined with size  $4 \times 2$  so the pseudo inverse is used. The condition number is a measure of the

Table 1. Useful states of the shutter. "0" indicates closed and "1" is open for pinholes A-D. State 4 is for science data-taking, with all pinholes closed. States 1, 2, 6, and 9 are for calibrating the speckles, with one pinhole open at a time. States 3, 5, 7, 8, 10, and 11 are for cross-calibrating the reference beams, with two pinholes open at a time.

State	A	B	C	D
1	0	0	1	0
2	1	0	0	0
3	1	1	0	0
4	0	0	0	0
5	1	0	1	0
6	0	1	0	0
7	0	1	1	0
8	0	1	0	1
9	0	0	0	1
10	1	0	0	1
11	0	0	1	1

amplification caused by the inversion of the matrix. In practice, the condition number is the ratio between the smallest and the largest singular values in the matrix.

In our observation scenario, 5 images are taken: one with the speckles and no reference beam, and four with speckles and each of the 4 reference beams in turn. (Each reference beam is engaged by opening the corresponding pinhole.) We derive an optimal solution for the speckle fields based on those five images; that optimal solution is characterized by the condition number, representing the degree to which the measurements are independent of each other and therefore constitute “rigid” constraints on the solution. If all 4 reference beams have similar optical phase at a particular pixel, there will be a high degeneracy between the 4 measurements in that pixel and thus a poor solution there (a large condition number). We explored a range of pinhole configurations and found one with a small maximum condition number. The value "3.17" means that the errors in the system (from measurement) will be amplified by 3.17 when applying the inversion. We do not claim that the pinhole locations we found are globally optimal, but they are adequate for our experiments.

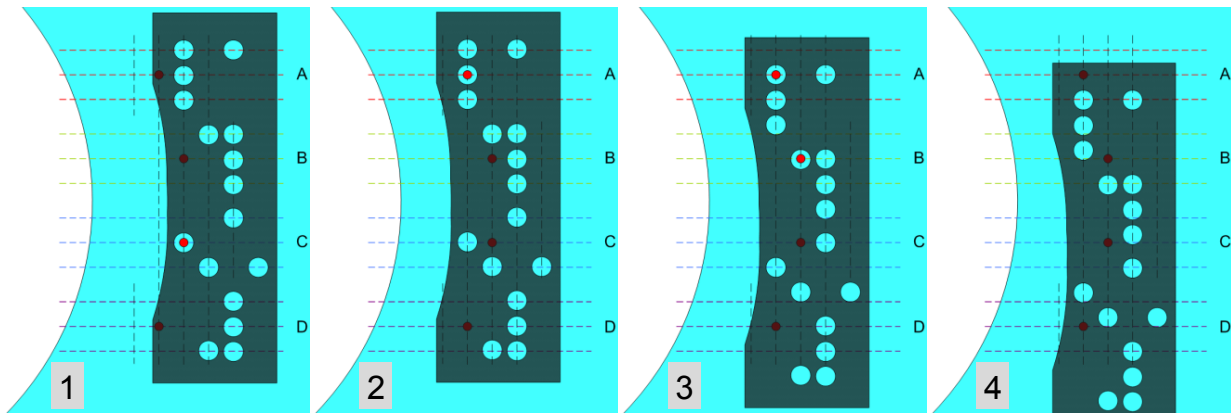


Figure 2. Sliding-mask shutter mechanism. With 3 vertical positions and 4 horizontal, the dark gray sliding mask offers 12 possible combinations of open/closed pinholes. Shown here are 4 of the 11 states we actually need: (1) Only pinhole C is open; (2) only pinhole A is open; (3) pinholes A and B are both open; and (4) none of the pinholes are open.

Currently our method uses 4 pinholes, and thus 5 images taken in succession. In theory, the minimum number of equations is 2 and it is possible to solve them with just two pinhole measurements. However, the periodicity of the diversity in the image plane from the tilted wavefronts originating at the pinholes creates regions of low diversity. For planet searches in a large dark hole, it is likely that at least 3 pinholes are required. For characterization of planets in a known region of the dark hole, two pinholes can be selected to give adequate diversity.

We open each pinhole in turn, or none of the pinholes, or combine them in pairs. With four holes to be switched on or off, this constitutes 11 states (Table 1). A sliding mask that moves on a 3×4 grid of positions (with two motorized translation stages) handles these 11 states (fig. 2). In each of these positions, the pinholes in the Lyot stop line up with 0, 1, or 2 holes in the moving mask.

A separate shutter blocks the entire “Football,” (the main Lyot opening). This may ultimately prove unnecessary, but for now we want a means of isolating each pinhole alone, for reference beam calibration without any stray light or speckle interference via the Football. In our experiments, we took a set of

diversity images (single pinhole plus open Lyot stop), and calibration images (Lyot stop closed and shutter moved to 10 open pinhole states) for each run. Depending on the system stability, it is not necessary to take calibration images each time.

This system of pinholes and moving masks was installed in HCIT in August, 2011. The only new hardware needed was a Lyot mask with four 300  $\mu\text{m}$  diameter holes, a sliding mask with 16 holes of 1 mm diameter, a sliding mask to block the football, and 3 linear actuators to move the masks.

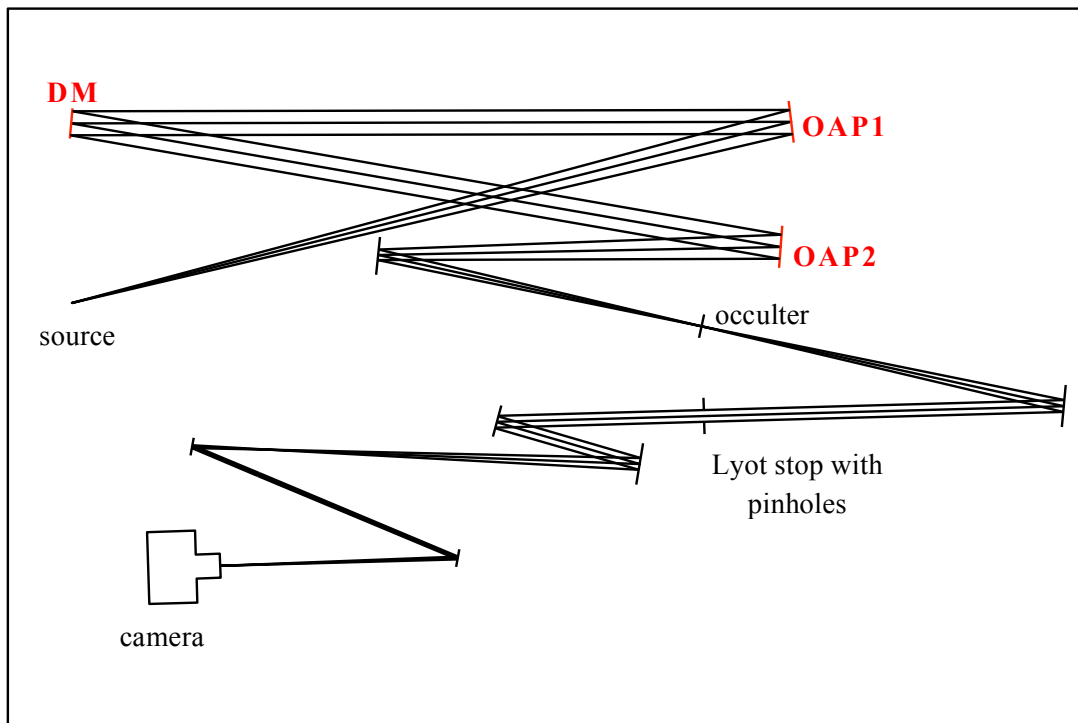


Fig. 3. Optical layout of Lyot table. The coronagraphic components, specifically the DM, occulter, and Lyot stop, are indicated. The system stop is a 48 mm aperture at the DM. The components that were replaced since the TPF-C Milestone #2 demonstration, the DM, OAP1, and OAP2, are shown in red.

### 3.2. HCIT Configuration: Changes Since TPF-C Milestone #2

The optical layout of the HCIT Lyot table for this experiment is slightly modified from the layout described in the TPF-C Milestone #2 report.<sup>1</sup> The first two off-axis parabolas (OAPs) and the DM have been replaced. The focal lengths of OAPs 1 and 2 were increased to 60 inches, a factor of 2 larger than the previous elements, and the 32x32 DM has been replaced with a 64x64-actuator DM (both DMs have a 1 mm actuator pitch). Figure 3 shows the new layout.

If using the full DM in both cases, the two configurations would have the same  $f/\#$  at the occulter while the new configuration would have twice as many actuators across the pupil. While the previous configuration used a 30 mm diameter stop to define the pupil (with 30 actuators spanning the diameter), the new configuration uses a 48 mm stop (48 actuators spanning the diameter), less than  $2\times$  the previous 30 mm stop. By increasing the focal length by  $2\times$  and the pupil diameter by  $1.6\times$ , the  $f/\#$  at the occulter is larger by a factor of approximately  $5/4$  than in the TPF-C Milestone #2 configuration.

We used the same focal plane mask that was used in TPF-C Milestone #2 experiments. This is a gradient-thickness nickel mask created by evaporating the nickel through a scanning slit. The transmission pattern is a  $1\text{-sinc}^2$  linear (not radial) profile convolved with a narrow Gaussian function to account for the finite width and proximity of the slit. The pattern was designed to have 50% transmission at  $4 \lambda/D$  at  $\lambda=800 \text{ nm}$ . With the new, slower beam, the 50% transmission point moved to  $3.2 \lambda/D$ . The transmission function is shown in fig. 4. In TPF-C Milestone 2, the Lyot mask was formed from the intersection of two circles each equal in diameter to the pupil stop, with the centers of the circles separated by  $\epsilon = 0.36$  of the pupil diameter. In the current experiment, we used  $\epsilon=0.34$ . After accounting for the larger  $f/\#$ , the new Lyot stop was more aggressive (larger pupil area) which helped maintain resolution but potentially raised the noise floor.

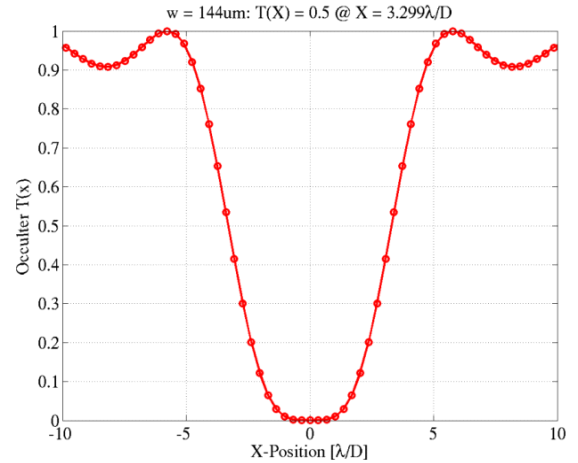


Figure 4. This is the designed TPF-C Milestone #2 mask transmission function with physical width  $w = 144 \mu\text{m}$  at the half-power point. With the new system  $f/\#$ , this point is at  $3.3 \lambda/D$  at  $\lambda = 800 \text{ nm}$ . The transmission at our inner working angle of  $4 \lambda/D$  is approximately 75%.

### 3.3. Broad Band Spectrum

The light source and filters used in our experiments were the same ones used to satisfy TPF-C Milestone #2. The light source was a single-mode supercontinuum photonic crystal fiber propagating high-power laser pulses. Non-linear interactions of the pulses and guiding structure lead to a broad spectrum that is shown in fig. 5. This spectrum was measured with an Ocean Optics spectrometer at the output of a single-mode (SM) fiber before it is connected to the SM fiber that runs into the vacuum chamber. Light is passed through each of the five bandpass filters, centered at roughly 768, 784, 800, 816, and 832 nm before entering the spectrometer. We have normalized the total measured power in all bands to be equal to one another as shown in the upper plot of fig. 5. We created an effective bandpass by summing together the 5 normalized bandpasses, as shown in the bottom plot. The spectrum is flat except where it appears that the 784 nm filter is shifted slightly toward the blue creating a peak at 776 nm and a valley at 791 nm. The full width at half-maximum (FWHM) of the synthetic spectrum spans 761.5 – 839.5 nm, leading to a FWHM bandwidth of 9.74% centered at 800.5 nm.

We give each filter equal weight in all of our broad-band analyses, so the bottom plot of fig. 5 is the effective spectrum of our experiment, modulo chromatic differences in quantum efficiency and throughput of the HCIT relative to the Ocean Optics spectrometer. These differences will be small over the individual 2% bandpass filters and will not significantly change the effective bandpass. Our results are nearly identical to those shown in figure 14 of the TPF-C Milestone #2 report.

We acknowledge that the 9.74% bandpass is just shy of the required 10% bandpass. This is the same spectrum that was used to satisfy TPF-C Milestone #2. Contrast loss generally scales as the square of the bandpass, so one would expect our results to be worse by about  $(10/9.74)^2 = 1.054$  had we used a full 10% bandpass. As will be shown below, our results had substantially more than 5% margin against the Milestone, so that the spectral underrun should not be an issue. Furthermore, in the TPF-C Milestone #2 report, Table 3 showed that a reweighting of the measured spectrum to an effective 10% bandpass yielded contrast results that differed by no more than  $10^{-11}$  of the equal-weighted results. The same difference is expected in our experiments.

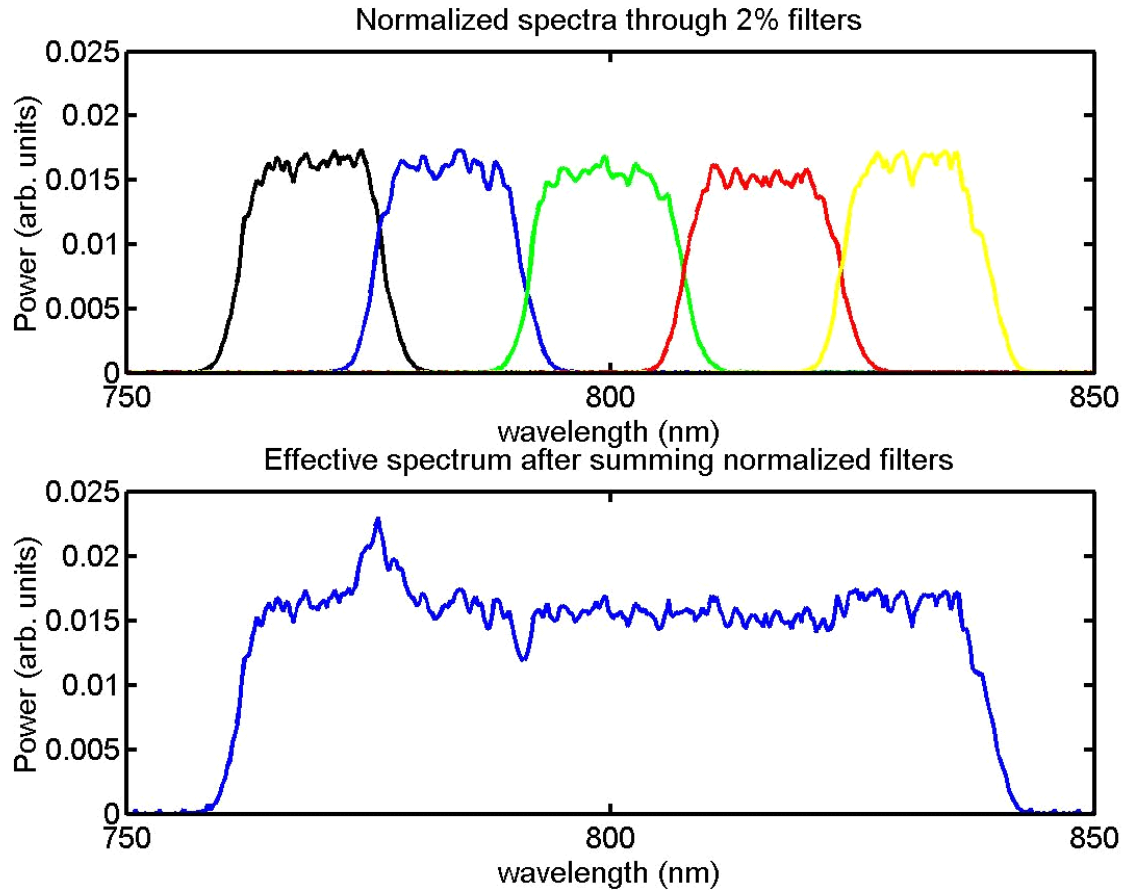


Figure 5. Top: we separately recorded the light through each of five 2% bandpass filters and have normalized all five to have the same total light. Bottom: we sum the recorded signals with equal weight to form an effective spectrum. The spectrum full-width half maximum spans 761.5–839.5 nm, leading to a spectrum centered at 800.5 nm with a bandwidth of 9.74%.

#### 4. MILESTONE PROCEDURES

This section contains the definitions, procedures, and requirements that comprise the ASSIC milestone demonstration, as specified in the ASSIC Milestone White Paper. The photometric normalization procedure has changed since TPF-C Milestone #2 and is explained in section 5.2. Editorial comments to the definitions are italicized.

## **4.1. Definitions**

The contrast metric requires a measurement of the intensity of speckles appearing within the dark field, relative to the intensity of the incident star. The contrast metric will be assessed in terms of statistical confidence to capture the impact of experimental noise and uncertainties. In the following paragraphs we define the terms involved in this process, spell out the measurement steps, and specify the data products.

### **4.1.1. “Raw” Image and “Calibrated” Image**

Standard techniques for the acquisition of CCD images are used. We define a “raw” image to be the pixel-by-pixel image obtained by reading the charge from each pixel of the CCD, amplifying and sending it to an analog-to-digital converter. We define a “calibrated” image to be a raw image that has had background bias subtracted and the detector responsivity normalized by dividing by a flat-field image. Saturated images are avoided in order to avoid the confusion of CCD blooming and other potential CCD nonlinearities. All raw images are permanently archived and available for later analysis.

### **4.1.2. Starting from scratch**

We define “scratch” to be a DM setting in which actuators are set to a predetermined surface figure that is approximately flat (typically, about 20 volts on each actuator). *We use focus diversity to determine the pupil phase. This is approximately the summed phase contributions from the optics between the point source and the camera, though it is dominated by the optics between the point source and the mask. We then set the DM to nominally flatten the system wavefront in the pupil. This is our ‘scratch’ setting. This means that the initial DM setting compensates the system aberrations and the DM is not itself flat, though the rms is ~4 nm and the p-v is ~60 nm.*

### **4.1.3. Testbed “star” source**

We define the “star” to be a small pinhole illuminated with broadband light relayed via optical fiber from a source outside the HCIT vacuum wall (e.g., the super-continuum white light source). The “small” pinhole is to be unresolved by the optical system; e.g., a 5- $\mu\text{m}$  diameter pinhole would be “small” and unresolved by the 40- $\mu\text{m}$  FWHM Airy disk in an f/50 beam at 800 nm wavelength. This “star” is the only source of light in the optical path of the HCIT. It is a stand-in for the star image that would have been formed by a telescope system.

For both Princeton and HCIT, illumination has a spectral passband of width  $\delta\lambda/\lambda_0 \geq 10\%$ , centered at a convenient wavelength  $\lambda_0$ , such as in the I spectral band,  $720 \text{ nm} \leq \lambda_0 \leq 880 \text{ nm}$ .

Some tests require a stray light source, which is incoherent with the star. This may be an LED near the detector, or an incandescent lamp outside the chamber, or even a sample of the “star” source carried with several cm of optical path delay. *The Princeton experiments are not part of this milestone report.*

### **4.1.4. Contrast map**

The “contrast map” is a dimensionless map representing, for each pixel of the detector, the ratio of its intensity value to the value at the peak of the central PSF that would be measured in the same testbed conditions (light source, exposure time, Lyot stop, etc.) if the coronagraph focal plane mask were removed.

#### **4.1.5. Speckle field map**

The speckle field map is a dimensionless complex-valued map representing the ratio of the optical electric field value at each pixel of the detector to the value at the peak of the central PSF that would be measured in the same testbed conditions (light source, exposure time, Lyot stop, etc.) if the coronagraph focal plane mask were removed. In the absence of stray light, the contrast map is proportional to the absolute value squared of the speckle field map; that is, the speckle field map combines the coherent portion of the contrast map with phase information. The calibration of the speckle field map is further detailed in section 4.2.

#### **4.1.6. Dark hole**

The dark hole is the region of the contrast map within which speckles are to be suppressed in preparation for CSD experiments. The dark hole chosen for this study is any useful  $2 \times 2 \lambda_0/D$  patch within  $<10 \lambda_0/D$  of the location of the star. [Sentence regarding old D-shaped region and Princeton experiment deleted.] *This was originally called “dark field” in the Milestone paper. We controlled the region  $(3, 12) \lambda_0/D$  in  $x$  and  $(-12, +12) \lambda_0/D$  in  $y$  in these experiments.*

#### **4.1.7. Contrast value**

The “contrast value” is a dimensionless quantity that is the average value of the contrast map over the  $2 \times 2 \lambda_0/D$  dark field adopted for the experiment. *We evaluated the contrast map in the region  $(4, 9) \lambda_0/D$  in  $x$  and  $(-9, +9) \lambda_0/D$  in  $y$  in these experiments.*

#### **4.1.8. Control algorithm**

We define the “control algorithm” to be the computer code that takes as input the PD-CSD measurements, and produces as output a voltage value to be applied to each element of the DM, with the goal of reducing the intensity of speckles. During this study we do not plan to develop a corresponding algorithm for Pinhole CSD measured speckle fields. *We did eventually do control with PH-estimated fields. We find that there is no significant difference in convergence between PD and PH estimated fields, at least to the  $10^{-9}$  contrast level.*

#### **4.1.9. Phase Diversity CSD measurement**

We define the “phase diversity coherent speckle detection (PD-CSD) measurement” to be the procedure implementing phase diversity CSD as a method of estimating each speckle’s amplitude and phase, including the changes applied to the DM and the computer code that takes calibrated images and yields estimates of speckle amplitude and phase. Using the results of the PD-CSD measurement to correct the wavefront is optional, as resources allow. *This may have been misstated in the white paper. PD measurements were exclusively used to correct the wavefront and form the dark hole. PH measurements were not used.*

#### **4.1.10. Pinhole CSD measurement**

We define the “Pinhole coherent speckle detection (PH-CSD) measurement” to be the procedure implementing PH-CSD (with a separated-path reference beam) as a method of estimating each speckle’s amplitude and phase, including the changes applied to the piston-tip-tilt mirror and the computer code that takes calibrated images and yields estimates of speckle amplitude and phase. Using the results of the PH-CSD measurement to correct the wavefront is optional, as resources allow.

#### 4.1.11. *Statistical Confidence*

The interpretation of measured numerical contrast values shall take into consideration, in an appropriate way, the statistics of measurement, including detector read noise, photon counting noise, and dark noise.

The milestone objective is to demonstrate with high confidence that the contrast map in the dark field, as estimated from PD-CSD measurements, matches the contrast map as estimated by the PH-CSD measurements, within 20% of the mean contrast value; and that the speckle phase determinations match within 1 radian. The contrast maps shall be obtained from the average of the set of four or more PD measurements in a continuous sequence, interleaved with an equal number of PH measurements.

Every pixel will have two comparable measurements (PD and PH) yielding a contrast map *difference*, in each of several iterations. The first thought is to treat every pixel in every iteration as an independent measurement of the contrast map difference, and to handle the statistics accordingly. This is reflected in the description below. But this isn't fully realistic: we also expect correlations across each contrast map, particularly within a PSF, which will reduce the number of truly independent samples that can be drawn from each map.

For this milestone the mean contrast value should be  $\sim 1 \times 10^{-8}$  in each PD measured contrast map, not as a primary performance criterion, but to establish conditions comparable to flight. Each PH measurement shall be accompanied by an adjacent PD measurement. The primary performance criterion is that the standard deviation of the PD-PH contrast differences shall be less than 20% of the contrast value with a confidence coefficient of 90% or better, and the mean of the PD-PH phase differences shall be less than 1 radian with a confidence coefficient of 90% or better.

Estimation of this statistical confidence level requires an estimation of variances. An analytical development of speckle statistics is impractical, since they include a mix of static speckles (the residual speckle field map remaining after the completion of a wavefront sensing and control cycle) and quasi-static speckles (arising from alignment drift following the control cycle); the superposition of speckles of multiple wavelengths exhibiting their own deterministic wavelength dependencies; and other sources of measurement noise including photon detection statistics and CCD noise. Our approach is to compute the confidence coefficients on the assumption of Gaussian statistics, but also to make the full set of measurements available to enable computation of the confidence levels for other statistics.

The average of one or more images taken at the completion of each iteration is used to compute the contrast map  $PD_{ij}$  for iteration  $i$  and pixel  $j$ . A PH-CSD measurement is made in an adjacent time period, representing the same pattern of speckles, and from that a contrast map  $PH_{ij}$  is derived. The mean contrast value for a given iteration  $i$  is:

$$C_i = \sum_{j=1}^n \frac{PH_{ij} + PD_{ij}}{2n} \quad (1)$$

where  $n$  is the number of independent pixels in the  $2 \times 2 \lambda_0/D$  selected dark field of each contrast map. Let us assume that the contrast difference  $\Delta_{ij} \equiv PH_{ij} - PD_{ij}$  is a Gaussian-distributed random variable drawn from a parent distribution of zero mean and width  $\sigma$ , where  $\sigma$  includes both technical errors in each

measurement and shot noise in the contrast maps. We can calculate the standard deviation in the contrast difference maps for each CSD iteration:

$$\sigma_{\Delta} = \sqrt{\sum_{i=1}^m \sum_{j=1}^n \frac{\Delta_{ij}^2}{mn-1}} \quad \text{where } \Delta_{ij} \equiv PH_{ij} - PD_{ij} \quad (2)$$

Our measured standard deviation  $\sigma_{\Delta}$  is an estimate of the parent uncertainty  $\sigma$ . We can calculate the probability density for getting a specific value  $\sigma_{\Delta}$  from a set of  $m \cdot n$  trials for a certain  $\sigma$ :

$$P(X)dX = \frac{mn}{\Gamma(1+mn/2)\sqrt{2^{mn}}} X^{mn-1} \exp\left(\frac{-1}{2} X^2\right) dX \quad \text{where } X \equiv \frac{\sigma_{\Delta} \sqrt{mn-1}}{\sigma} \quad (3)$$

We can integrate this to find the probability that  $\sigma \leq \sigma_0$ , where  $\sigma_0$  is the performance goal, in our case 20% of the mean contrast value. This gives

$$P(\sigma < \sigma_0; \sigma_{\Delta}, mn) = \frac{mn}{\Gamma(1+mn/2)\sqrt{2^{mn}}} \int_{X_0}^{\infty} X^{mn-1} \exp\left(\frac{-1}{2} X^2\right) dX \quad \text{where } X_0 \equiv \frac{\sigma_{\Delta} \sqrt{mn-1}}{\sigma_0} \quad (4)$$

This is the statistical confidence level that the measured standard deviations in Eq. 2 meet the goal with sufficient margin. It can be evaluated in closed form for any integer  $m \cdot n$ . For several values of  $m \cdot n$  we can plot the probability vs.  $\sigma_{\Delta}/\sigma_0$ . This tells us the ratio by which  $\sigma_{\Delta}$  must be better than the goal (smaller), to know the parent  $\sigma$  is also below the goal with a particular confidence level.

#### 4.2. Photometric Normalization

All images with the coronagraph fully assembled are normalized to the unocculted star peak brightness, i.e., an unocculted image would reach a normalized intensity of 1.0 at the peak. With the coronagraph fully assembled, normalized intensities across an image typically range from  $10^{-4}$  down to  $10^{-10}$ .

A simple one-step calibration technique would be to image the unocculted star with a short exposure, record its peak, then linearly scale that peak with exposure time and assume stability of the source brightness. However, this would require linearity over  $> 10^6$  range of exposure times and would be limited by 1-2% source variability on minutes timescales and  $> 10\%$  variability over days timescales. The solution used in TPF-C Milestone #2, and in this experiment, is to perform a

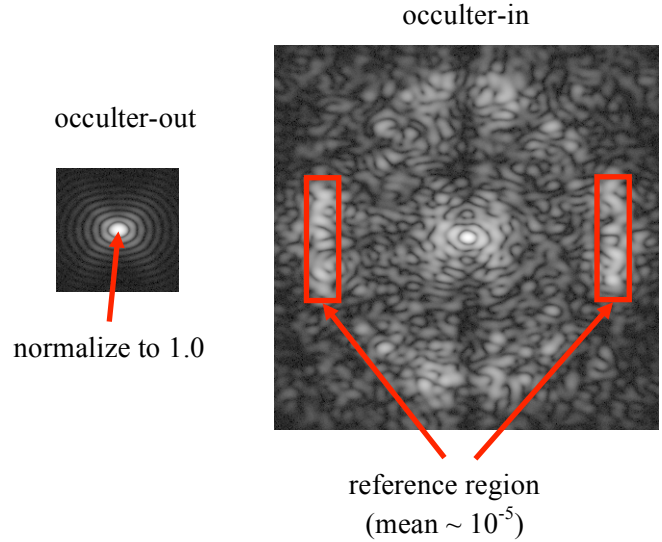


Fig. 6. (LEFT) Unocculted star, (RIGHT) assembled coronagraph image. The reference region is located  $25-28 \lambda/D$  away from the star, where the DM has little effect. The reference region brightness is calibrated to the unocculted star brightness, then every coronagraph image uses the reference region for normalization.

Technology Milestone Whitepaper  
Advanced Speckle Sensing for Internal Coronagraphs – Shaklan

calibration of the brightness of a reference region of the coronagraph science plane image relative to the unocculted star brightness, then normalize each subsequent fully assembled coronagraph image to the brightness of the reference region contained in the same image (see fig. 6). Because this reference region is imaged concurrently with the rest of the coronagraph field, the stability of the source brightness and the linearity of exposure times have no effect on the normalization.

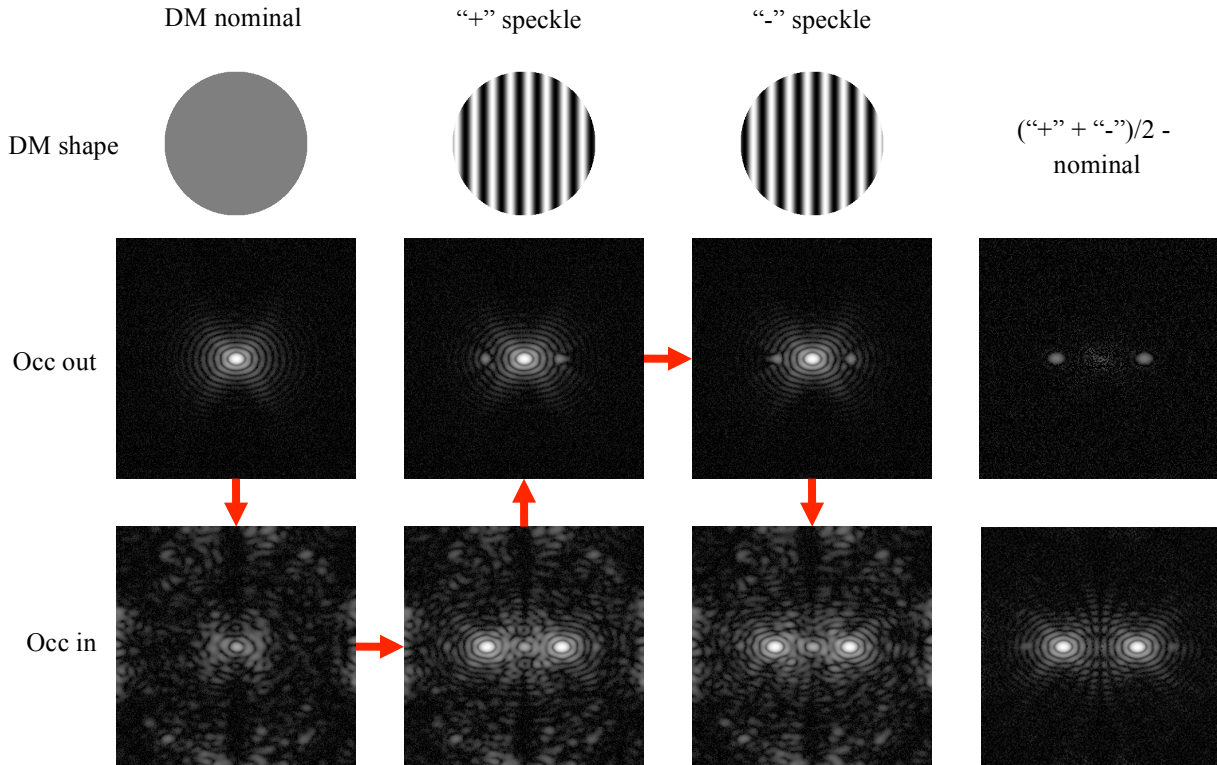


Fig. 7. Sequence of images used to establish photometric relationship between unocculted star and “reference region.” All intensity images are log-scaled, and the occulter-in images are  $\sim 1000\times$  brighter both in integrated source flux and in display stretch. Each image spans  $\pm 25 \lambda/D$  in  $x$  and  $y$ . The sequence begins at the top-left image, with the occulter out and the DM set to a nominal shape. The sequence is established by moving the occulter in or out at each DM setting, then moving to the next DM setting, adding a “+” speckle or a “-” speckle (shown by following the red arrows). The difference images (shown in the right-hand panels) contain, to first order, only the intensity of the dynamic speckle field added by the DM. The occulter-out dynamic speckle field is related to the occulter-in dynamic speckle field by the occulter intensity transmission, which is well measured at these separations (near the transmission maximum).

The reference region of the image is chosen to be in a location that is bright enough to be well measured, but far enough out in the PSF so that it is affected little by changes in the DM. The features in the unocculted images in the region spanning  $25\text{-}28 \lambda/D$  are dominated by the diffraction rings of the on-axis star, which are exactly the features that the fully assembled coronagraph removes. This means that there are no easily isolated features that are common to both the unocculted and fully assembled coronagraph images to establish the relationship between them.

While the use of a calibrated reference region to normalize subsequent images is the same in this experiment as it was for TPF-C Milestone #2, the method used for initial calibration has changed. The TPF-C Milestone #2 calibration technique relied on a sequence of images, alternating between changing total illumination and changing occulter positions. Each step in that sequence which changed the occulter position relied on source stability to tie together successive exposures; with  $\sim 1\text{-}2\%$  source variability on short timescales, used on  $\sim 4$  steps, the resulting uncertainty was in the range of 4%. The technique adopted in this experiment eliminates the dependence on source stability, trading it for a dependence on DM linearity and hysteresis. The hysteresis and departures from linearity, while each affecting the DM motion at  $\sim 4\%$  levels, are expected to result in calibration errors at  $\sim 1\%$  levels, as described below. While the accuracies of the previous calibration technique,  $\sim 4\%$ , and the current technique,  $\sim 1\%$ , are both acceptable, the initial calibration technique adopted in this experiment is preferred.

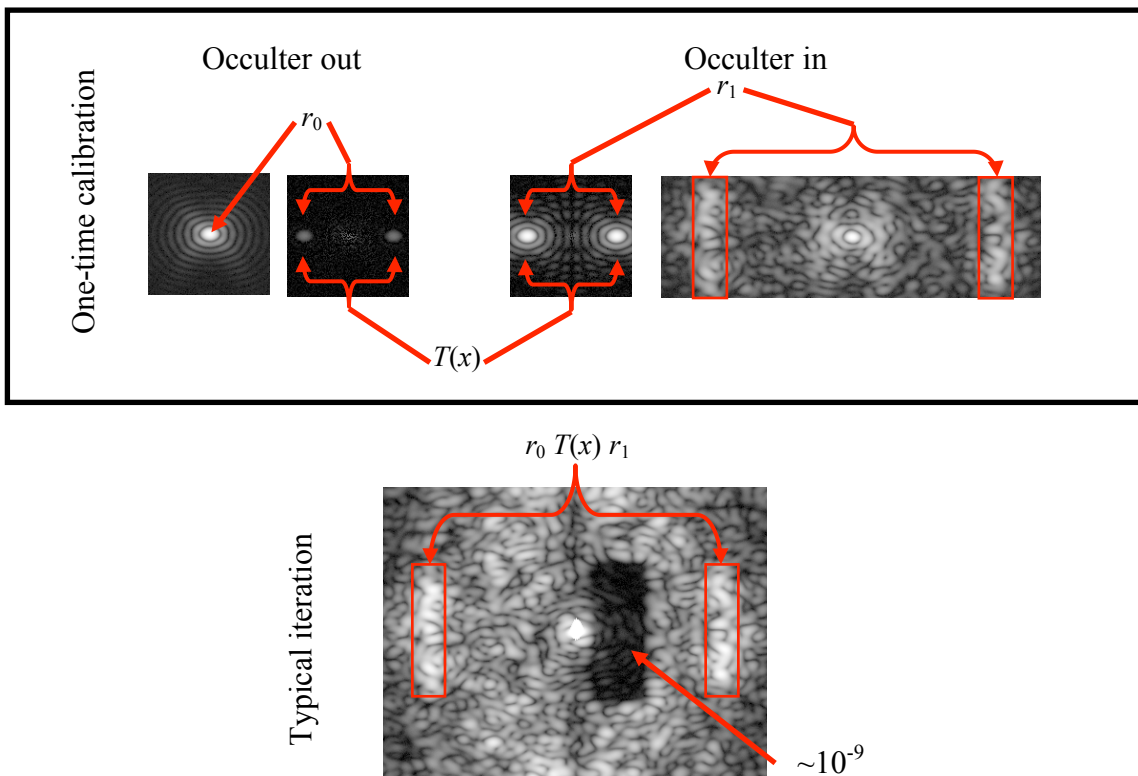


Fig. 8. Photometric calibration relationships and usage. The top panels show steps in the one-time calibration establishing the reference region. The measurement of  $r_0$  and  $r_1$  are ratios of the dynamically added speckles relative to the unocculted peak and reference region brightnesses, respectively, and typically come to  $10^{-3}$  and  $10^{-2}$ . The occulter-out dynamic speckles are related to the occulter-in dynamic speckles by the occulter intensity transmission at the location of the speckles,  $T(x) \sim 0.91$  (transmission relative to maximum transmission). In every image afterwards (e.g., bottom panel), the observed reference region brightness is scaled to  $r_0 T(x) r_1$ , implying an equivalent unocculted peak brightness of 1.

To perform the initial calibration of the relative brightnesses of the unocculted peak intensity and the reference region of a fully assembled coronagraph image, the DM is used to create a dynamic speckle pattern across a sequence of images (see fig. 7). This speckle pattern is visible both in the unocculted and fully assembled coronagraph images, and by choosing DM patterns with opposite signs (i.e., a “+” pattern and a “-” pattern), the underlying “nominal” intensity pattern has no influence on the difference signal, to limits set by DM hysteresis and nonlinearities. Briefly, at any given point in the unocculted image, if the initial  $E$ -field is  $E_0$ , the nominal intensity is  $|E_0|^2$ , and the difference image formed by  $(|E_0 + \Delta E_{DM}|^2 + |E_0 - \Delta E_{DM}|^2)/2 - |E_0|^2 = |\Delta E_{DM}|^2$ . A sample sequence of images is shown in Fig. 7, clearly demonstrating that the features in the left-hand panels are absent from the right-hand panels. The DM hysteresis and nonlinearity re-introduce a sensitivity to  $E_0$  through the cancelled “cross-term”  $2\text{Re}\{E_0\Delta E_{DM}\}$ , which for reasonable errors in the unocculted images come to  $\sim 1\%$  of  $|\Delta E_{DM}|^2$ . This systematic error is smaller than the typical random error, which in practice comes to about 1.7% rms without any averaging of separate images or sequences.

The difference in observed brightness of a dynamic speckle in the unocculted images and the same speckle observed in the fully assembled coronagraph, is simply the occulter transmission at the location of that speckle. For this reason, the location of the dynamic speckles is chosen to be near the occulter transmission maximum, where uncertainty in the transmission is negligible. The sequence of images that establishes the photometric calibration relies only on relative brightnesses of concurrently measured features (i.e., different locations in the same image) and on knowledge of the occulter intensity transmission at the location of the dynamic speckles.

The photometric calibration bridges the range of intensities from 1.0 at the unocculted peak, to  $10^{-3}$  for the dynamic speckles, to  $10^{-5}$  for the reference region. Once the photometric calibration is established for the reference region, intensities down to the  $10^{-9}$  level can be measured with a  $\text{SNR} \geq 1$  per pixel per image, in images that do not saturate the reference region (see fig. 8). By increasing exposure times and allowing the reference region to saturate, and by averaging over multiple exposures, intensities at the  $10^{-10}$  level can be measured with  $\text{SNR} > 1$  per pixel. Given the current  $f/\#$  and an 800 nm center wavelength,  $f\lambda/D \sim 6$  pixels, the noise level per resolution element is typically well below  $10^{-10}$ .

### **4.3. Success Criteria**

This section is extracted from the ASSIC White Paper. Editorial comments not present in the white paper are italicized.

#### **4.3.1. Light source**

Illumination is spectrally broadband in single or dual polarization, with a bandwidth  $\delta\lambda/\lambda_0 > 10\%$  centered at a convenient wavelength  $\lambda_0$ , such as in the range  $720 \text{ nm} \leq \lambda_0 \leq 880 \text{ nm}$ . *In this experiment, as in TPF-C Milestone 2, the bandwidth resulting from our 5 filter set and supercontinuum source was 9.74% (Sect 3.3). The expected performance over a full 10% bandpass would be about 5% worse, well within the margins of our results relative to the milestone.*

*Rationale:* Wavelengths in this range are representative of the science band used by future missions. The bandwidth, although less than would be used in a flight mission, provides an appropriate challenge for this milestone.

#### **4.3.2. Contrast performance**

As a starting point for measurements, a mean contrast value less than  $1 \times 10^{-8}$  should be achieved in a  $2 \times 2 \lambda_0/D$  region centered at any convenient location  $< 10 \lambda_0/D$  from the star position. *During wavefront control, the individual filter band contrast maps were measured and ranged in contrast by about a factor of 2. The central bands were below  $1 \times 10^{-8}$  contrast, the outer bands were above it (see Appendix III). We measured and controlled the contrast in a region that was larger than the final  $5 \times 18 \lambda_0/D$  scoring region. We stopped the control when the estimated average contrast in the controlled region was  $10^{-8}$ . The scored region was determined later. Thus there was not a clean way to insure that the average contrast in the scored region would be below  $10^{-8}$ . In one case (see Table 3), the average contrast over the scored region was  $1.14 \times 10^{-8}$ . In 5 of the 6 cases, the average contrast was less than or equal to  $1 \times 10^{-8}$ .*

The contrast maps as measured by PH and PD measurement shall match with a standard deviation of 20% of the contrast value, with 90% confidence. The speckle field phase measurements by these two methods shall match with a standard deviation of 1 radian with 90% confidence. *Results are reported in Section 5.3. Statistical confidence is verified in Section 5.4. Contrast maps are shown in Appendix III.*

In the series of interleaved wavefront measurements and DM corrections using PH and PD, described in Section 3.5 [of the ASSIC Milestone white paper], each cycle will be preceded and followed by equivalent time series of open-loop measurements taken at the same baseline contrast. These additional measurements will allow the open-loop stability of speckles in the testbed to be characterized. *This was done by first controlling the contrast, the last iteration of which was the first PD estimate at the beginning of open loop contrast. We then did a PH estimate, followed by a PH calibration (fig. 9), and then a second PD estimate. The first PD estimate occurs just before PH estimation for all runs listed in Table 2. The time of the first PD estimate is not shown in the table. The time between PD estimates was  $\sim 3$  hours from the last PD control estimation to the post-PH PD estimation. We consistently found that the contrast in the two PD estimates agreed to 5% r.m.s. in the scored region. This is a measure of the open loop stability over the duration of each run. The goal of our experiment was to show agreement between PH and PD measurements – the result is about 14% r.m.s. in the scored region (Table 3). Our PD repeatability measurements show that the testbed stability was not a limiting factor in the PH vs. PD experiment.*

These success criteria shall be quantified in terms of the standard deviation of differences and statistical confidence defined in Eqs. 2 and 4 of Section 4.1.11. *Reported in Section 5.4.*

*Rationale:* The mean contrast is low enough to be in the same optical regime as normal science observations. The uncertainty is comparable to the desired fractional uncertainty for calibration and subtraction of the speckle pattern to reveal a planet. Phase accuracy below 1 radian helps speed closed-loop convergence.

#### **4.3.3. Incoherent stray light background**

The tests described in Section 4.3.2 will be repeated with added uniform incoherent stray light brighter than the mean speckle contrast (nominally  $1 \times 10^{-8}$  of the star's peak). The contrast maps measured by CSD in the presence of added stray light (but excluding that DC offset) must match those measured by CSD without added stray light, with a standard deviation of 20% of the contrast value, with 90% confidence. The speckle field phase measurements likewise must match with a standard deviation of 1 radian with 90% confidence. *We realized during experimentation that there was an unfortunate inconsistency with*

Technology Milestone Whitepaper  
Advanced Speckle Sensing for Internal Coronagraphs – Shaklan

*this success criterion. The first sentence calls for a repeat of the contrast demonstration in 4.3.2, but with the incoherent stray light turned on. That is what we did in full compliance with the specified procedures. The second and third sentences call for a comparison of the contrast with and without the background lights turned on. That is a different test that does not compare PD and PH, but compares for example PD measurements with and without the background light. The white paper does not define a procedure for such a test. We have performed an iteration of this test and achieved 8% agreement (Section 5.3, Table 3, and Appendix III), in the presence of  $3 \times 10^{-8}$  additive background light, far exceeding the 20% requirement.*

*Rationale:* This demonstrates the milestone performance with stray light, one of the key measurement challenges. *Our incoherent stray light tests showed that the PD and PH estimates remained consistent with one another in the presence of background lights. Results are reported in Section 5.3 with statistical verification in Section 5.4. Contrast maps are shown in Appendix III.*

**4.3.4. Duration and robustness**

Criteria 4.3.2 and 4.3.3, averaged over the data set, shall be met with a confidence of 90% or better, as defined in Section 4.1.11. Sufficient data must be taken to justify this statistical confidence. *Section 5.4.*

*Rationale:* Until we attempt to close the wavefront control loop using CSD measurements, the rms difference of contrast measurements obtained from this dataset provides our best estimate of the contrast measurement uncertainties. Assuming the contrast differences have a Gaussian distribution about zero, this demonstrates a statistical confidence of 90% that the CSD contrast measurement goal has been reached.

Criteria 4.3.2 and 4.3.3 must be satisfied on three separate occasions with a reset of the wavefront control system software (DM set to scratch) between each demonstration. *This was done over the course of 2 days for 4.3.2, and over two more days for 4.3.3. See Table 2, figures 9, 10 and 11.*

*Rationale:* This provides evidence of the repeatability of the contrast measurement demonstration. The wavefront control system software reset and re-optimization between data sets ensures that the three data sets can be considered as independent and do not represent an unusually good configuration that cannot be reproduced. For each demonstration the DM will begin from a "scratch" setting and the algorithm used to converge will have no memory of settings used for prior demonstrations, so that we can expect the speckles to be measured are quite different each time. There is no time requirement for the demonstrations, other than the time required to meet the statistics stipulated in the success criteria. There is no required interval between demonstrations; subsequent demonstrations can begin as soon as prior demonstrations have ended. There is also no requirement to turn off power, open the vacuum tank, or delete data relevant for the calibration of the DM influence function.

**4.3.5. Certification Process**

From the ASSIC White Paper, the text here gives the requirements of the Milestone Certification Data Package. New comments are italicized.

The Principal Investigator will assemble a milestone certification data package for review by the Exoplanet Exploration Program (ExEP) and its Technology Advisory Committee (ExEP-TAC). In the event of a consensus determination that the success criteria have been met, the ExEP will submit the findings of the ExEP-TAC, together with the certification data package, to NASA HQ for official

certification of milestone compliance. In the event of a disagreement between the ExEP and the ExEP-TAC, NASA HQ will determine whether to accept the data package and certify compliance or request additional work.

#### **4.3.6. Milestone Certification Data Package**

The milestone certification data package will contain the following explanations, charts, and data products, with estimates of accuracy where appropriate.

1. A narrative report, including a discussion of how each element of the milestone was met, an explanation of each image or group of images, appropriate tables and summary charts, and a narrative summary of the overall milestone achievement. *Section 5.*
2. A description of the optical elements, their significant characteristics, and their layout in the HCIT. *Sections 3.1 and 3.2.*
3. A tabulation of the significant operating parameters of the apparatus, including temperature stability. *See fig. 11 for DM shape, and Appendix II for temperature. No other parameters are reported.*
4. A calibrated image of the reference star, and an estimate of photometry errors. *Section 4.2.*
5. Calibrated images of the occulter transmittance pattern and/or the measured transmittance profile. *Figure 4, Section 3.2.*
6. Spectrum of the broadband light and an estimate of the intensity uniformity and stability of the illumination reaching the defining pupil (at the DM). *Figure 5, Section 3.3. The intensity was measured to be stable to +/-10% p-v over several hours. With the new normalization approach (sect 4.2) the contrast measurement is independent of the source intensity. Instead it relies on the stability of the scattering regions, which was found to be highly stable over the course of all the experiments.*
7. A contrast map image representative, within error limits, of the super set of data, with appropriate numerical or color-coded or grey-scale coded contrast values indicated, and with coordinate scales indicated in units of Airy distance ( $\lambda_0/D$ ); and the corresponding contrast map for the CSD determination in an adjacent time period. *Section 5.1, figure 10 for the coordinate scales. Appendix III for the PD and PH contrast maps.*
8. A phase map image representative, within error limits, of the super set of data, with appropriate numerical or color-coded or grey-scale coded contrast values indicated, and with coordinate scales indicated in units of Airy distance ( $\lambda_0/D$ ); and the corresponding phase map for the CSD determination in an adjacent time period. *Section 5.1, figure 10 for the coordinate scales. Appendix III for the PD and PH phase maps.*
9. The PH-PD phase difference standard deviation for the  $2 \times 2 \lambda_0/D$  target area for each data set comprising several consecutive iterations, and for all relevant data sets, in tabular form. *Table 3. We used a  $5 \times 18 \lambda_0/D$  target area.*
10. The PH-PD contrast difference standard deviation with vs. without stray light, for the  $2 \times 2 \lambda_0/D$  target area for each data set comprising several consecutive iterations, and for all relevant data sets, in tabular form. *Table 3. We used a  $5 \times 18 \lambda_0/D$  target area.*

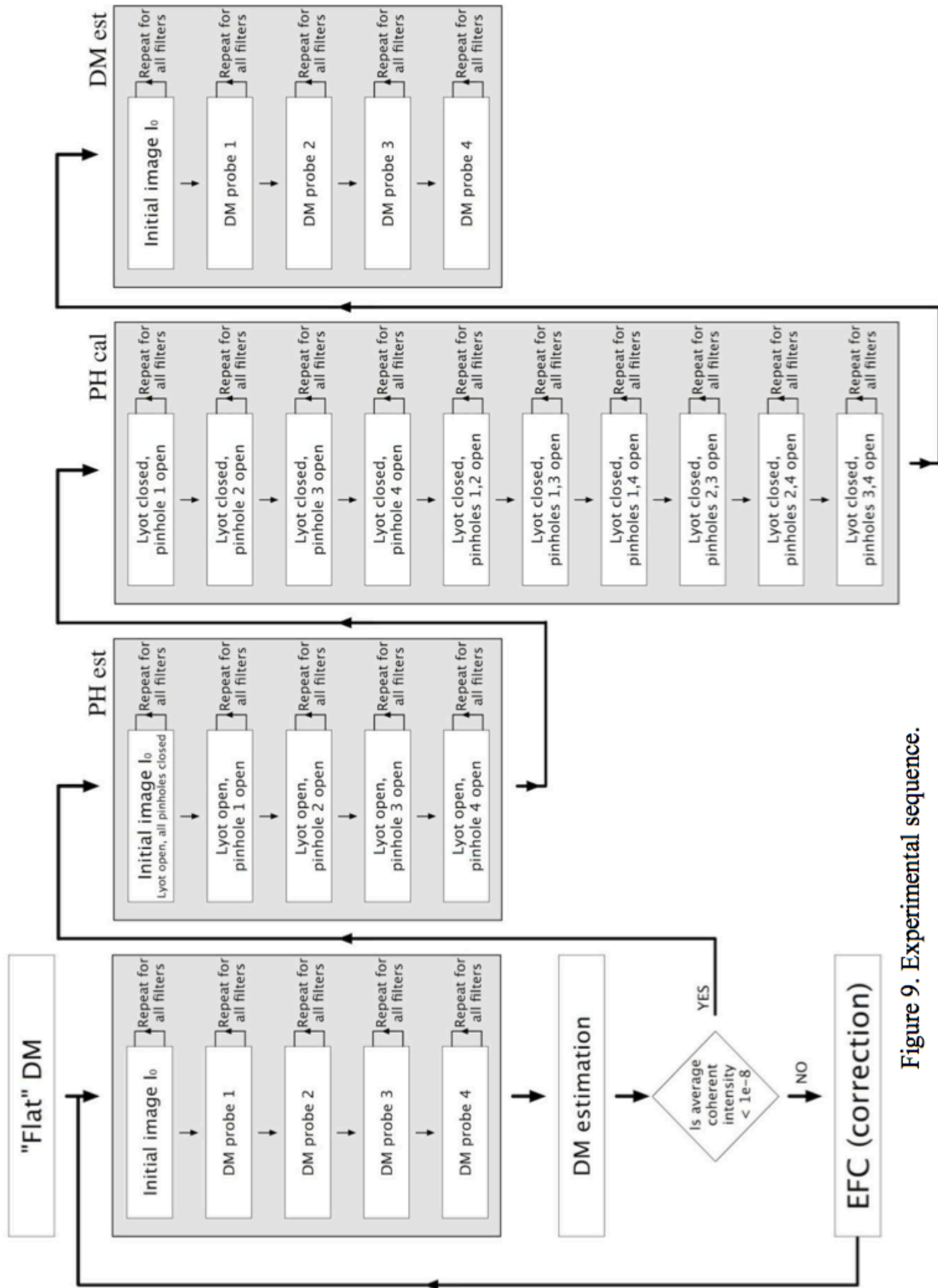


Figure 9. Experimental sequence.

## 5. NARRATIVE REPORT

### 5.1. Data Acquisition

Each data acquisition run consisted of the following four steps:

- Resetting the DM to initial condition (“scratch”) which is a DM configuration that corresponds to a flattened phase in the Lyot plane from defocus diversity. The resulting contrast in the dark zone is roughly  $10^{-6}$ .
- Running Electric Field Conjugation (EFC) using DM-based estimation and correction over the five 2% bands until coherent contrast within the dark zone dropped below  $10^{-8}$ . Record the DM configuration. The five bands are measured one at a time and given equal weight to synthesize a 10% broad band image. All five bands are used in the contrast estimate and contribute to the DM control setting. We used 2% bands rather than a single 10% band because it provides the control algorithm with the wavelength-dependent aberration information that allows it to perform broad-band correction.
- Keep the DM at this recorded configuration and take intensity measurements in the image plane first with the main opening in the Lyot stop open and all pinholes blocked. Then four intensity measurements with the main opening open and each of the pinholes open, one at a time. Then, blocking the main opening of the Lyot stop and taking four intensity measurements with each of the pinholes open. Then, lastly, keeping the main opening blocked and taking six intensity measurements of all the possible pairs of pinholes open.
- Starting from the recorded DM configuration, taking one image (as before), letting light through the main opening of the Lyot stop (all pinholes blocked). Then taking four intensity images with the DM changed to produce the change in the electric field according to the DM-based estimation.

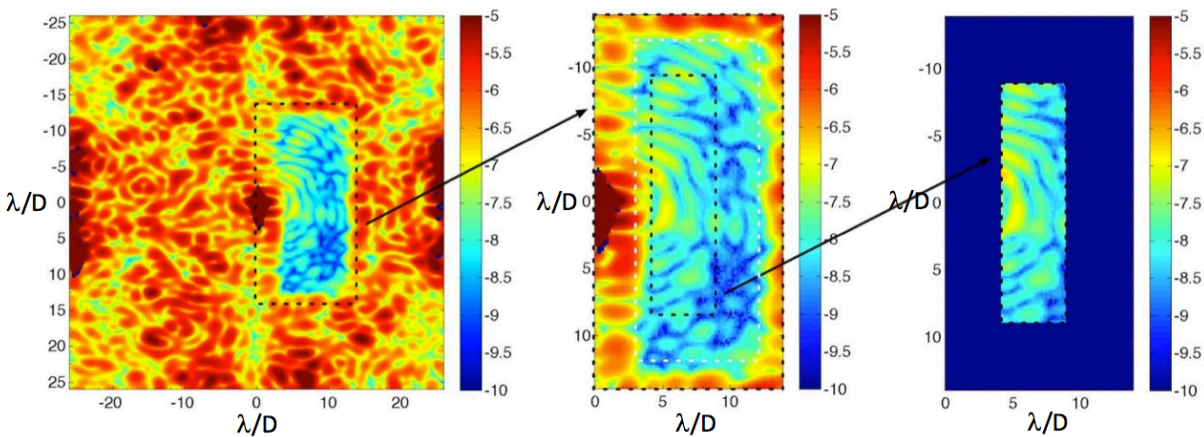


Figure 10. Left: This is the full field seen by the science camera using one of the 2% bandwidth filters. We correct one side of the image plane. Our control matrix includes the region within the black-dashed rectangle extending to about  $13 \lambda/D$ . The same physical region (same camera pixels) are used for all 5 filters. Middle: We control the region inside the white dashed rectangle extending from 3 to 12 (horizontal) and from -12 to 12 (vertical)  $\lambda/D$ . Right: we evaluate the contrast in this TDEM within the black rectangle extending from 4 to 9 (horizontal) and -9 to 9 (vertical)  $\lambda/D$ . The figures in Appendix III show this region for all 5 filters.

Technology Milestone Whitepaper  
Advanced Speckle Sensing for Internal Coronagraphs – Shaklan

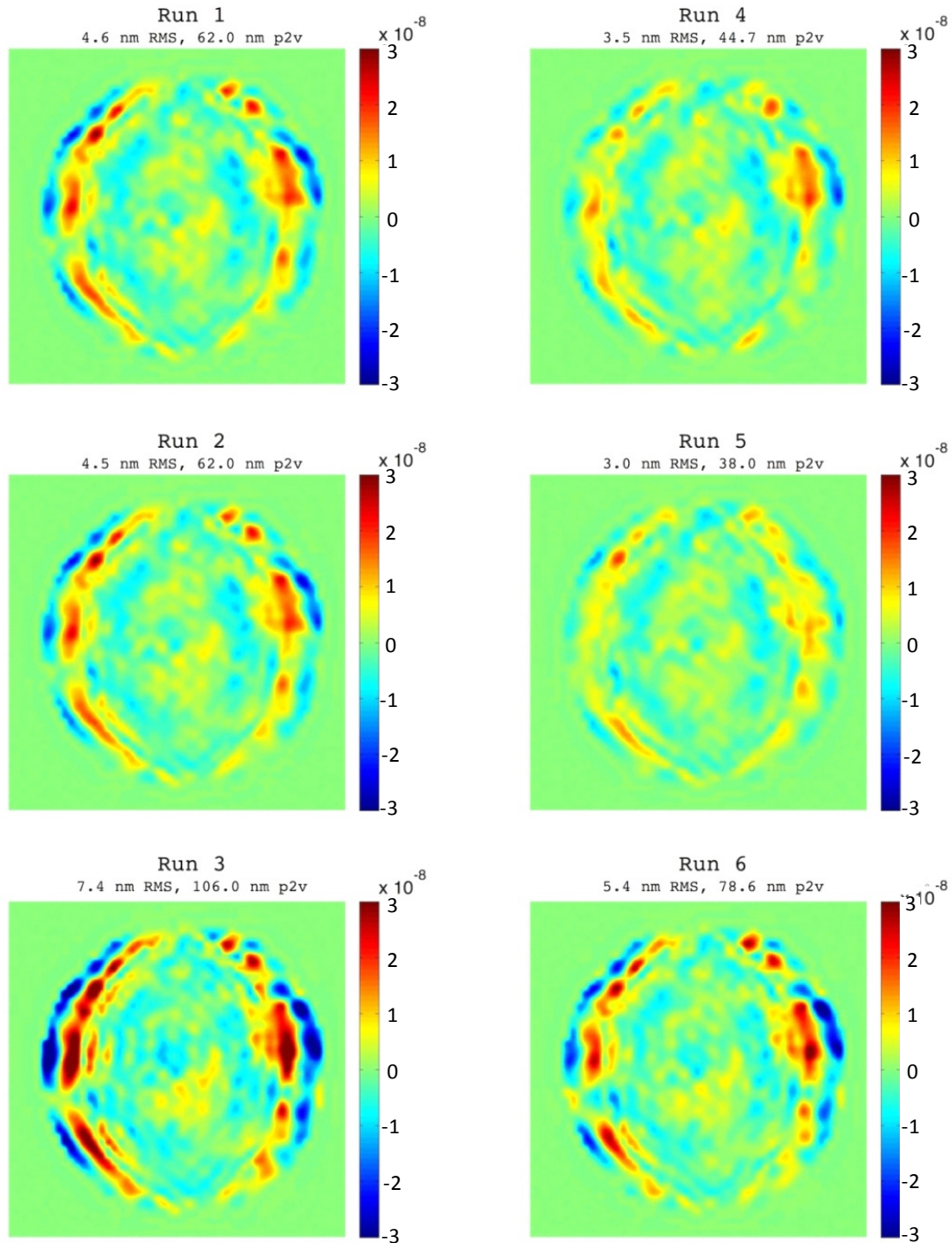


Figure 11. DM settings for  $10^{-8}$  contrast for the six milestone runs.

The data collection sequence is shown schematically fig. 9 and the wavefront control region is shown in fig. 10. The process of starting from scratch, controlling the wavefront, collecting PH calibration data, PH estimation data, and PD estimation data typically took about 3 hours to complete. This was mainly driven by the sequential recording of 5 wavebands. Trauger *et al*<sup>11</sup> have had success with wavefront control using 6-7% bandwidth filters<sup>10</sup> which would considerably reduce the wavefront estimation and control times.

Technology Milestone Whitepaper  
 Advanced Speckle Sensing for Internal Coronagraphs – Shaklan

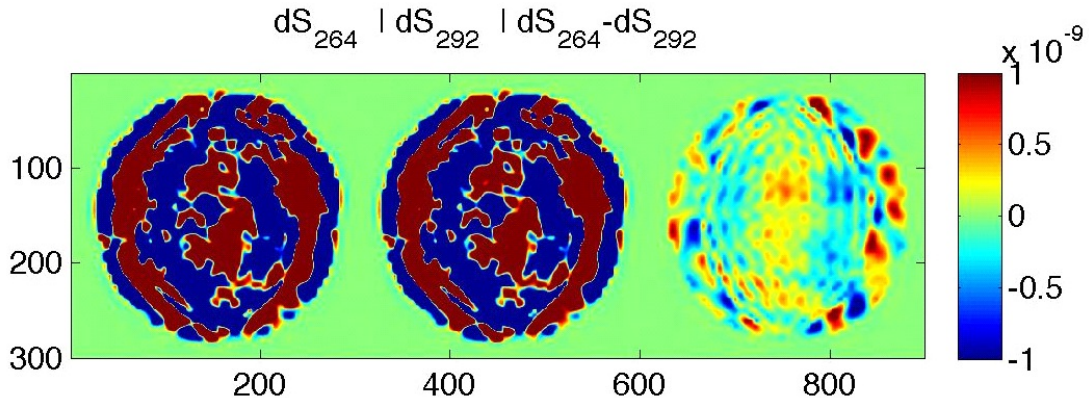


Figure 12. DM surface for run 1 and run 2, and the surface-height difference map. Full scale color shown is  $\pm 1$  nm. After setting the DM to scratch, the dark hole is optimized until a contrast of  $10^{-8}$  is achieved. For the first two runs, the final solutions were very similar, differing only by about 2 nm p-v.

Table 2. Experiment operating parameters

Run	Itr	Mode	Start time	Elaped time (sec)	exposure time per frame (sec)	Number of frames per image	DM surface change from flat rms (nm) / p2v (nm)
1	218	flat	2012-01-17T11:32:17				
	262	PH est	2012-01-18T08:10:59	1768	5	5	
	263	PH cal	2012-01-18T08:40:28	7084	35	3	
	264	DM	2012-01-18T10:38:33	1708	3	5	4.6 / 62.0
2	265	flat	2012-01-18T12:23:14				
	290	PH est	2012-01-18T15:44:09	1767	5	5	
	291	PH cal	2012-01-18T16:13:37	7087	35	3	
	292	DM	2012-01-18T18:28:29	1710	3	5	4.5 / 62.0
3	293	flat	2012-01-18T18:57:00				
	326	PH est	2012-01-19T00:59:21	1771	5	5	
	327	PH cal	2012-01-19T01:28:52	7091	35	3	
	328	DM	2012-01-19T03:27:04	1717	3	5	7.4 / 106.0
4	436	flat	2012-01-20T16:27:20				
	516	PH est	2012-01-20T23:26:33	1626	2	6	
	517	PH cal	2012-01-21T01:52:04	7104	35	3	
	518	DM	2012-01-21T01:52:04	1815	2	6	3.5 / 44.7
5	523	flat	2012-01-21T17:45:09				
	614	PH est	2012-01-22T09:41:05	1630	2	6	
	615	PH cal	2012-01-22T10:08:16	7109	35	3	
	616	DM	2012-01-22T12:06:45	1819	2	6	3.0 / 38.0
6	617	flat	2012-01-22T22:59:01				
	684	PH est	2012-01-23T11:04:19	1628	2	6	
	685	PH cal	2012-01-23T11:31:28	7107	35	3	
	686	DM	2012-01-23T13:29:56	925	2	2	5.4 / 78.6
7	870	flat	2012-01-25T11:27:24				
	1023	PH est	2012-01-27T10:18:18	2267	3	8	
	1024	PH cal	2012-01-27T10:56:06	7109	35	3	
	1025	DM	2012-01-27T12:54:35	2459	3	8	6.4 / 86.1

Technology Milestone Whitepaper  
 Advanced Speckle Sensing for Internal Coronagraphs – Shaklan

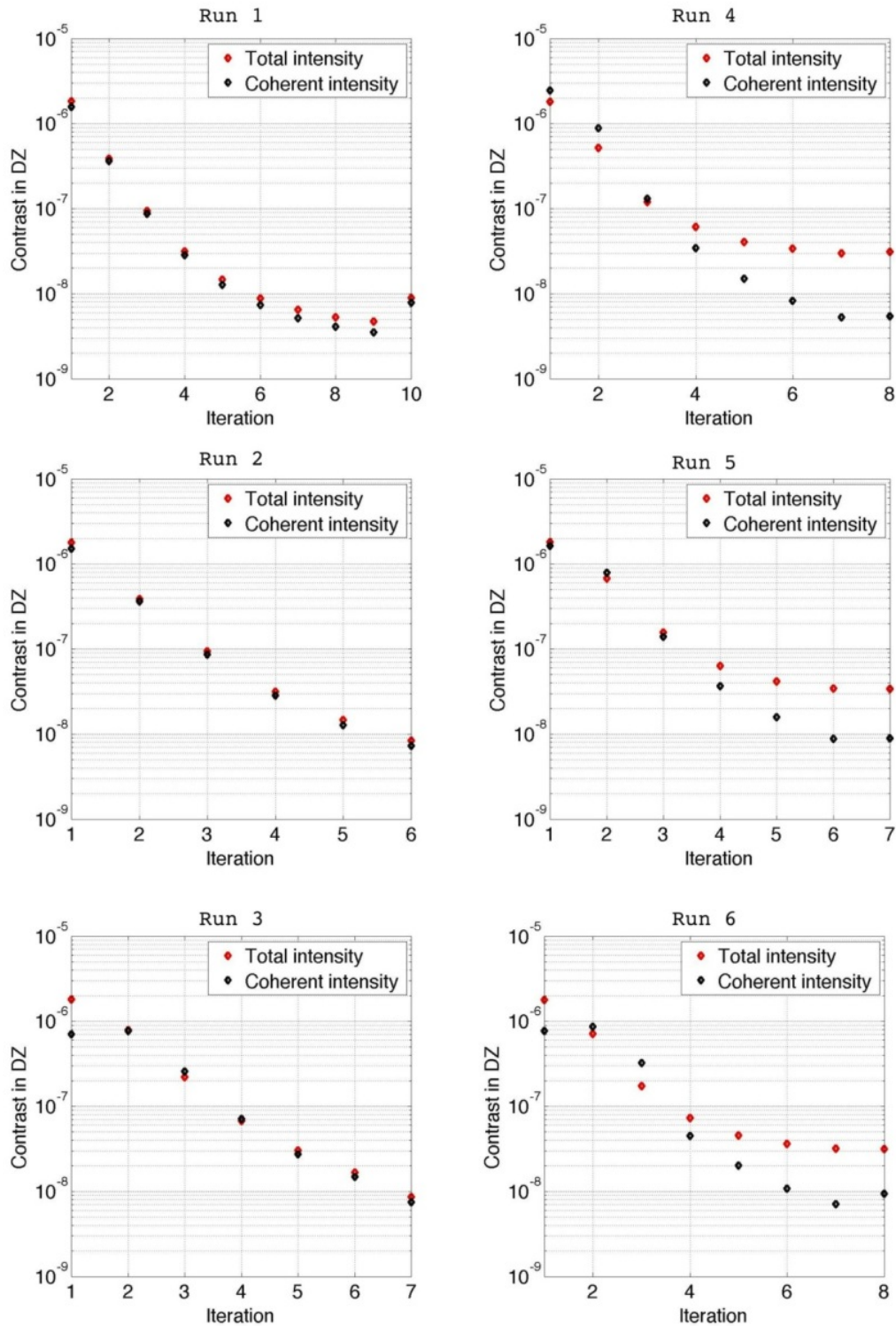


Figure 13. Contrast vs. Phase Diversity control iteration. The process starts with a nominally flat wavefront in the pupil and contrast  $\sim 10^{-6}$  in the dark hole. After several iterations in which the contrast in all 5 filters is controlled, the coherent (controllable) contrast is at  $\sim 10^{-8}$ . In runs 4-6, the background light level is  $\sim 2.0 \times 10^{-8}$ .

We collected 6 sets of data to satisfy the milestone. The first three were collected with no background lights inside the tank. The second set of three had a background lamp turned on (conveniently, an optical encoder inside one of our actuators), providing a  $1.5 \times 10^{-8}$  uniform background across the dark hole. Table 2 lists the data runs, time stamps, elapsed times, and other experimental data. Note that a seventh run is included. We repeated the experiment with no background light, but at deeper contrast ( $\sim 4 \times 10^{-9}$  over the dark hole).

Figure 11 shows the commanded DM shape after convergence to  $10^{-8}$  contrast. The images show the characteristic ringing around the outside of the Lyot stop that is typical of broad-band control.<sup>12</sup> The first two DM solutions are very similar to one another (see figs. 12), indicating that the testbed was stable and the DM hysteresis was negligible, leading to nearly identical starting points. This is not too surprising given the good thermal stability of the tank (see Appendix for thermal data). The four other solutions are different from one another, indicating a slightly different initial condition and alignment after the DM was reset to “scratch” each time.

The convergence plots for each of the 6 milestone runs are shown in fig. 13. The initial contrast with the DM set to ‘flat’ is  $\sim 10^{-6}$ , typically converging to  $10^{-8}$  contrast after 8 iterations. In run 1, we exceeded  $10^{-8}$  contrast (too deep for the milestone definition) so we reset the DM to an earlier iteration and then performed the experiment. Runs 4-6 show that the total intensity is  $\sim 2 \times 10^{-8}$  higher than the estimated coherent contrast. This is due to the additive background light.

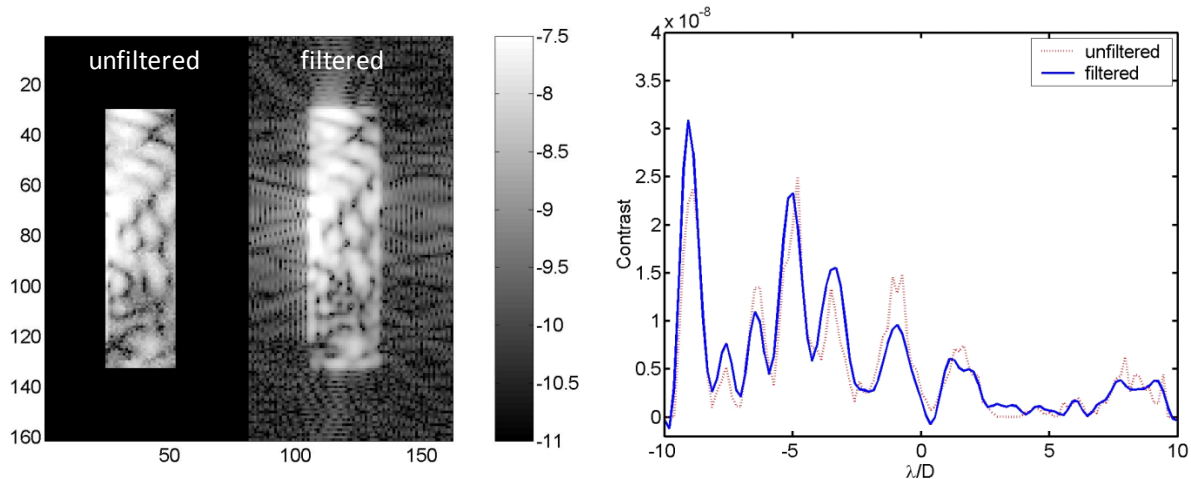


Figure 14. An example of PH contrast estimation at 800 nm in unfiltered data, and after low-pass filtering to a resolution of  $0.5 \lambda/D$ . Left: the region  $(-4 -9, -9 -9) \lambda/D$  is shown in log-scale pre- and post-filtering. Right: a vertical cut through the filtered and unfiltered image. The filtering removes pixel noise with no loss of spatial resolution.

## 5.2. Low-Pass Filtering of Image Plane Data

The image-plane estimates are constructed on a pixel-by-pixel basis. With pixel scales ranging from 5.6 to 6.1 pixels per  $\lambda/D$ , the dark hole images are oversampled with respect to the image-plane morphological features. The image-plane  $E$ -fields are, by construction, band-limited to spatial frequencies corresponding to scales  $> \lambda/D$  (defined by the Lyot stop), and the intensities to scales  $> (\lambda/D)/2$ . The measurements used to construct the estimates have a significant white noise component

(e.g., CCD read noise and Poisson noise), whose high spatial frequency components are easily discriminated from optical features. Here we have used a simple hard-edged spatial frequency cutoff low-pass filter, corresponding to  $(\lambda/D)/2$  spatial scales, resulting in no loss of spatial resolution in the underlying  $E$ -fields and intensities. All estimates reported below have been low-pass filtered using a hard edged filter prior to analysis for milestone compliance. The smoothing effect of the filter is shown in fig. 14. The filter introduces ringing primarily at the edge of the masked region. This ringing is as large as 20% of the intensity in the edge pixels, but to the extent that PH and PD images are similar, the ringing is also similar. At the edge of the region, it has about a 4% effect on the difference between the PD and PH images. The overall effect in the dark hole region is much less. All contrast results reported below have been low-pass filtered to  $0.5 \lambda/D$  resolution prior to analysis for milestone compliance.

### 5.3. Results

Our results are summarized in Table 3. Experiments are labeled 1-8 and are identified (for internal use) by the HCIT iteration number (column 2, 'itr'). The experiments are separated into three groups. First, runs 1-3 are with no additive background light. Runs 4-6 are with the additive background light turned on, and run 7 was a repeat of the test with no background light but at an overall higher contrast than the milestone runs. Run 8 is a comparison of PD estimation with and without background lights. Because of their size, the contrast and phase maps for each of these runs are attached in the appendix of this report.

The coherent contrast (column 4) is estimated over a dark hole spanning  $(4, 9) \lambda/D$  in  $x$  (normal to the mask contours) and  $(-9, +9) \lambda/D$  in  $y$  (along mask contours). The values in column 4 are the mean of the estimated coherent contrast determined by the PD and PH measurements, after averaging over the five 2% filters uniformly weighted to synthesize a 10% bandpass. The terms "PD" and "PH" here represent the contrast inside the low-pass filtered dark hole. From the ASSIC TDEM white paper, the mean is given by

$$C = \sum_{j=1}^m \frac{PH_j + PD_j}{2m} \quad (1)$$

where  $m$  is the number of independent pixels. Note that we have changed notation slightly from the white paper:  $m$  is the number of pixels, whereas  $n$ , introduced below, is the number of statistically independent estimates, or speckles, in the image.

Table 3. Measured contrast

Run	itr	Background light	Est. Coherent Contrast x 1e-8	Uncontrolled Contrast x 1e-8	PD-PH rel. inten. error std. dev.	PD-PH phase std. dev. Radians
1	262, 264	off	0.93+/-1.13	0.11	14%	0.23
2	290, 292	off	0.87+/-1.04	0.11	13%	0.25
3	326, 328	off	1.00+/-1.03	0.12	12%	0.25
4	431, 433	on	0.95+/-1.02	2.6	12%	0.27
5	614, 616	on	1.14+/-1.26	2.5	15%	0.46
6	684, 686	on	0.95+/-0.96	2.5	15%	0.40
7	1023, 1025	off	0.39+/-0.34	0.08	13%	0.43
8	2330, 2331	on vs off	0.62+/-0.61	3	8%	0.24

The residual uncontrolled contrast (column 5) is the part of the total measured light that does not respond to the probes, i.e. residual uncontrolled contrast = total contrast – estimated coherent contrast. The uncontrolled light is a combination of both additive background light not originating with the point source, and uncontrolled coherent light. Some of the coherent light remains uncontrolled because of wavelength-dependent propagation and dispersive imperfections in the system that are not compensated by the DM with its finite number of degrees of freedom, as well as polarization and time-variability in the system. The background light is responsible for the difference between the uncontrolled light level in runs 4-6 and runs 1-3, about  $1.5 \times 10^{-8}$ .

The column “PD-PH rel. inten. error std. dev.” is the measured fractional standard deviation  $\sigma_{\Delta}$  of the difference of the estimated coherent intensity from the PD and PH estimates and is computed from

$$\sigma_{\Delta} = \frac{1}{c} \sqrt{\sum_{j=1}^n \frac{(\Delta_j - \bar{\Delta})^2}{n-1}} \quad \text{where } \Delta_j = PH_j - PD_j \quad (2)$$

and  $\bar{\Delta}$  is the mean of the contrast difference. As noted above,  $n$  is the number of independent estimates in the dark hole. The value of  $n$  used in our analysis will be explained below in the Statistical Confidence section.

Finally the last column of Table 3 is the standard deviation of the phase difference of the two estimated fields. The phase maps were determined independently to within a constant by the PD and PH techniques. The constant, which is the offset between the pinhole and main Lyot stop phases, was measured by exposing pinhole A and the Lyot Stop while blocking B, C, and D, and performing PD estimation in the five spectral bands to estimate the complex field. We then repeated with all pinholes closed. This allowed us to determine the phase due to pinhole A relative to the phase with the Lyot Stop alone. The relative phases of B, C, and D to A were determined from the pinhole calibrations. The table shows the worst-case among the five bands analyzed for each broadband run. To calculate the standard deviation, we first subtract the estimated PD phases from the PH phases, then unwrapped the differences by adding or subtracting  $2\pi$  so that they are all between  $-\pi$  and  $\pi$  before computing the standard deviation.

#### 5.4. Statistical Confidence

First we determine the approximate number of independent image plane estimates,  $n$ , that are used in our computation of the contrast difference and phase difference between the pinhole and phase diversity estimates. For a given measured standard deviation,  $\sigma$ , large  $n$  improves the confidence in the estimate of the true standard deviation  $\sigma$ . The milestone requirement calls for an experiment that achieves  $\sigma < 0.2$  with 90% confidence.

To determine  $n$ , we consider the size and shape of the Lyot stop (which tells us the size and shape of the PSF), the area of the dark hole being analyzed, and the width of the spatial filter used in analyzing the image plane. The Lyot stop is formed by the intersection of two circles each with diameter equal the pupil diameter  $D$ . The centers of the two circles are separated by a fraction  $\epsilon=0.34$  of the pupil diameter, so that the open width is  $0.66D$  wide and the height is  $\sim 0.85D$ . The PSF scales inversely with these dimensions and has a FWHM of approximately  $1.51 \times 1.18 \lambda/D$ . The equivalent area of the PSF is then  $1.51 * 1.18 * \pi / 4 = 1.4 (\lambda/D)^2$ .

Technology Milestone Whitepaper  
Advanced Speckle Sensing for Internal Coronagraphs – Shaklan

The area that we analyze is the region  $x = (4, 9) \lambda/D$ ,  $y = (-9, +9) \lambda/D$ . This is an area  $90 (\lambda/D)^2$ . The number of independent degrees of freedom is roughly equal to the number of independent PSF images or “speckles” in the image plane, or  $90/1.4 = 64$ . We conservatively adopt  $n=60$  as the number of independent measurements in our confidence limit calculation.

In the milestone white paper we showed that the statistical confidence level that the true standard deviation  $\sigma$  is less than the goal  $\sigma_0$  for a measured standard deviations  $\sigma$ , is

$$P(\sigma < \sigma_0; \sigma_\Delta, n) = \frac{n}{\Gamma(1 + n/2)\sqrt{2^n}} \int_{X_0}^{\infty} X^{n-1} \exp\left(-\frac{1}{2} X^2\right) dX \quad \text{where} \quad X_0 \equiv \frac{\sigma_\Delta \sqrt{n-1}}{\sigma_0} \quad (3)$$

where  $n$  is the number of independent points ( $n=60$ ). Our milestone definition calls for  $P>0.9$  that  $\sigma < 0.2$ . In figure 15 we plot  $P$  for several values of  $n$ , and for different ratios  $\sigma_D/\sigma_0$ .

From figure 15, we see that for  $P=90\%$  confidence with  $n=60$ , we require  $\sigma_s < 0.89 \sigma_0$ , or  $\sigma_s < 0.178$  for  $\sigma_0=0.2$ . Our experimental results in Table 3 show that for runs 1-3 with no additional background light, the worst case contrast difference achieved was  $\sigma_s=14\%$ , thus  $\sigma_s/\sigma_0 = 0.70$  and  $P>0.9998$ . When the background light was turned on, the worst case contrast difference achieved was  $\sigma_s=15\%$ , yielding  $P=0.998$ . *Thus we have comfortably achieved the milestone with no worse than 99.5% confidence that the true standard deviation of the difference between the pinhole and phase diversity estimates is  $< 20\%$ .*

The phase requirement is to show that  $\sigma < 1$  radian with 90% confidence. For no background light, the worst case for all 6 runs had  $\sigma_s = 0.46$  resulting in  $P>0.999999$ . We thus easily meet the phase difference criterion.

We also did an experiment to compare the estimated contrast using phase diversity with background lights on and background lights off. This is labeled ‘run 8’ in Table 3, and the contrast and phase maps are presented at the end of Appendix III. We found that the contrast estimates were in agreement to 8% while the phase estimates agreed to 0.37 radians at the worst-case bandpass. The additive background level was  $3 \times 10^{-8}$ . This measurement was made from ‘scratch’ as were the PD-PH comparisons. The measurement process was not prescribed in the white paper, so we followed the approach of the PD-PH procedure, controlling in all 5 bands and stopping the control when the average contrast across the 10% band reached  $10^{-8}$ .

## 6. CONCLUSION

In broad-band light, the experiment repeatedly achieved 14% disagreement at  $10^{-8}$  contrast, easily meeting the milestone requirement. We repeated the experiment at a deeper contrast,  $4 \times 10^{-9}$ , and achieved 13% disagreement. Further experimentation at still deeper contrast is required to determine the PH-PD agreement noise floor.

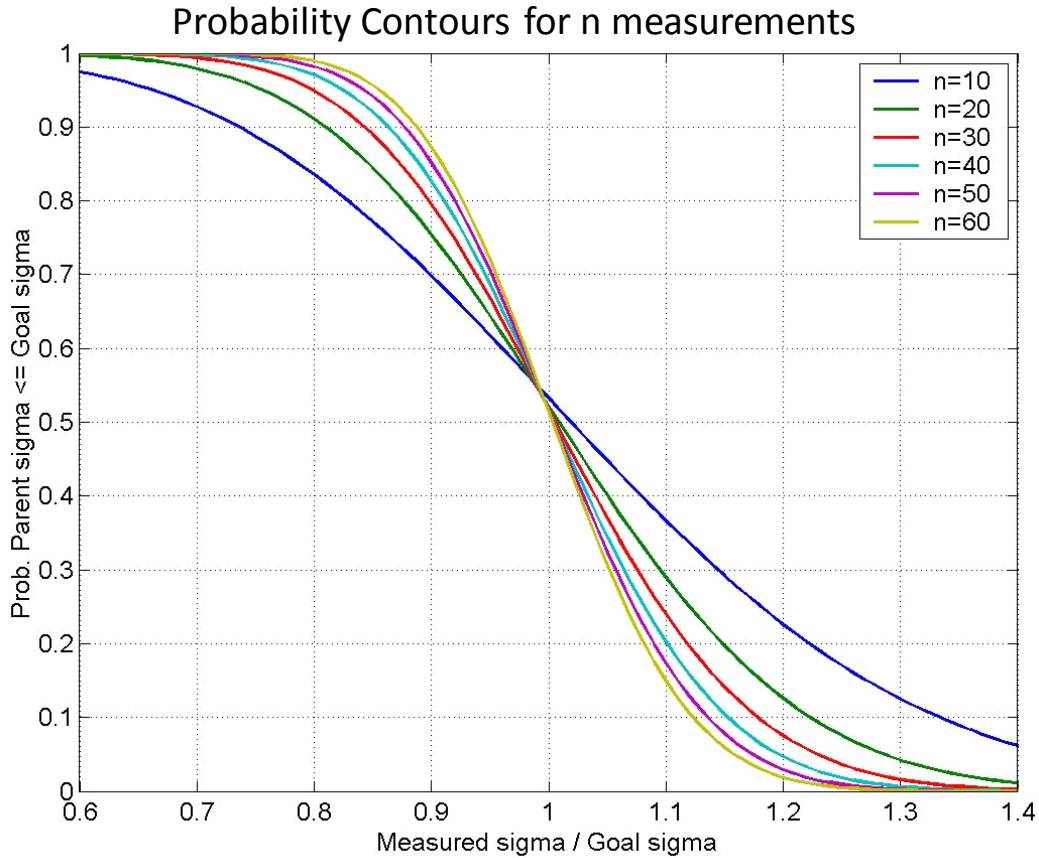


Figure 15. Probability contours for  $n$  independent measurements. To achieve 90% confidence that the true standard deviation is better than the goal, the measured  $\sigma_{\Delta}$  must be less than goal such that the contour line for  $n$  is above 0.9. With  $n = 60$ , the measured standard deviation should be no more than 89% of the goal standard deviation. If the measured standard deviation is  $\sigma_{\Delta} = 15\%$  and the goal is  $\sigma_0 = 20\%$ , then with  $n = 60$ , the confidence is  $> 99.8\%$  that the true standard deviation is  $< 20\%$ .

The two electric field estimation approaches used in this work are quite different from one another. The PD technique derives its diversity from actuating the DM. The interference field from the probe pattern is uniform across the dark hole, and its overall phase changes from one probe to the next. The PH technique places a static, tilted wavefront across the image plane, forming interference fringes whose phase changes linearly across the dark hole. These two independent estimation approaches agree to a contrast level of  $0.13 \times 4 \times 10^{-9} = 5 \times 10^{-10}$  across the 10% bandpass.

On the other hand, as seen in the contrast plots in Appendix III, the PH-PD disagreement of individual 2% bands was between 12 and 27% (with one outlier at 34%). The ‘good’ and ‘bad’ agreement is random from filter to filter between runs.

Why isn’t the agreement better? We spent some time exploring this question and will report on it in detail at a conference. We were able to estimate the self-consistency of the pinholes by imaging single pinholes (4 images) and pairs of pinholes (6 images) to solve for a 7-parameter model (1 pinhole

amplitude, 3 relative pinhole amplitudes, 3 relative pinhole phases). We found that the difference between the measurements and the model was ~10%, which explains much of the disagreement between the PH and PD measurements. Currently our best guess at explaining the 10% self-inconsistency of the pinholes is that our binary mask isn't positioned precisely enough to expose the image plane with pinhole light exactly the same way at each position (e.g. when we expose pinholes 1 and 2 together, there could be a slight clipping of the light from one or both of them that is different from when they are individually exposed).

We thank Marie Levine, Roger Linfield, Peter Lawson, and the ExEP Technical Assessment Committee for critical readings and comments that helped improve the quality of this document.

## 7. REFERENCES

1. B. Kern, A. Kuhnert, & J. Trauger, "Exoplanet Exploration Coronagraph Technology Milestone #2 Report," JPL Document D-60951, Aug 8, 2008.
2. J. Trauger & w. Traub, "A laboratory demonstration of the capability to image an Earth-like extrasolar planet," *Nature* 446, 771-773 (2007).
3. W. Sparks and H. Ford, "Imaging spectroscopy for extrasolar planet detection," *Ap. J.* 578, 543-564 (2002).
4. J. Krist, S. Shaklan, & M. Levine, "Extraction of extrasolar planet spectra from realistically-simulated, wavefront-corrected coronagraph fields," *Proc. SPIE* 7010, 701044-1 (2008).
5. P. Baudoz *et al*, "The self-coherent camera: a new tool for planet detection," *Proc. IAU Colloq.* 200, 553-558 (2005).
6. R. Galicher, P. Baudoz, & G. Rousset, "Wavefront error correction and Earth-like planet detection by a self-coherent camera in space" *A&A* 488, L9-L12 (2008).
7. R. Galicher *et al*, "Self-coherent camera as a focal plane wavefront sensor: simulations," *A&A* 509, A31 (2010).
8. A. Give'on, *et al*, "Broadband wavefront correction algorithm for high-contrast imaging systems", *Proc. SPIE* 6691, 66910A (2007).
9. S. Kendrick *et al*, "Technology Milestone White Paper Advanced Speckle Sensing for Internal Coronagraphs," JPL Document D-68673. Originally published April 29, 2011. Revised Nov. 28, 2011.
10. C. Noecker, et al, "Advanced Speckle Sensing for Internal Coronagraphs," *Proc. SPIE* 8151, 81510I (2011).
11. J. Trauger *et al*, "A hybrid Lyot coronagraph for the direct imaging and spectroscopy of exoplanet systems: recent results and prospects", *Proc. SPIE* 8151, 81510G (2011).
12. D. Moody & J. Trauger, "Design and demonstration of hybrid Lyot coronagraph masks for improved spectral bandwidth and throughput," *Proc. SPIE* 7010, 70103P-1 (2008).

## APPENDIX I. PINHOLE BASED ESTIMATION

Given a complex electric field in the final image plane of the coronagraph,  $E_0$  and the ability to independently let light through four different pinholes on the side of the main opening of the Lyot stop, we can model the intensity of light in the image plane for five different cases as

$$\begin{aligned}
 I_o &= |E_0|^2 + I_{inc} \\
 I_{oa} &= |E_0 + E_a|^2 + I_{inc} \\
 I_{ob} &= |E_0 + E_b|^2 + I_{inc} \\
 I_{oc} &= |E_0 + E_c|^2 + I_{inc} \\
 I_{od} &= |E_0 + E_d|^2 + I_{inc}
 \end{aligned} \tag{A1}$$

where  $I_o$  is the intensity of light for the case where all 4 pinholes are blocked and light only goes through the main opening of the Lyot mask,  $I_{oa}$ ,  $I_{ob}$ ,  $I_{oc}$  and  $I_{od}$  represent the intensity of light for the four cases where the main opening of the Lyot mask is open and one of the pinholes, a, b, c or d, respectively, is open.  $E_a$ ,  $E_b$ ,  $E_c$  and  $E_d$  are the electric fields in the image plane due to the light going through each of the pinholes, respectively, and  $I_{inc}$  is the incoherent light in the system that goes through the main opening of the Lyot stop. Unlike the pair-wise estimation technique used with the deformable mirror, these set of equations are exact and not an approximation due to the linearity of the optical system. Given a model description of the optical path to each of the pinholes, their location and size, it is possible to model the expected electric field due to each of the pinholes and then solve for  $E_0$  using the following relationship with measurements of the intensity of light of the five cases above:

$$\begin{bmatrix} \Re\{E_0\} \\ \Im\{E_0\} \end{bmatrix} = \frac{1}{2} \begin{bmatrix} -\Im\{E_a\} & \Re\{E_a\} \\ -\Im\{E_b\} & \Re\{E_b\} \\ -\Im\{E_c\} & \Re\{E_c\} \\ -\Im\{E_d\} & \Re\{E_d\} \end{bmatrix}^{-1} \begin{bmatrix} I_{oa} - |E_a|^2 \\ I_{ob} - |E_b|^2 \\ I_{oc} - |E_c|^2 \\ I_{od} - |E_d|^2 \end{bmatrix} \tag{A2}$$

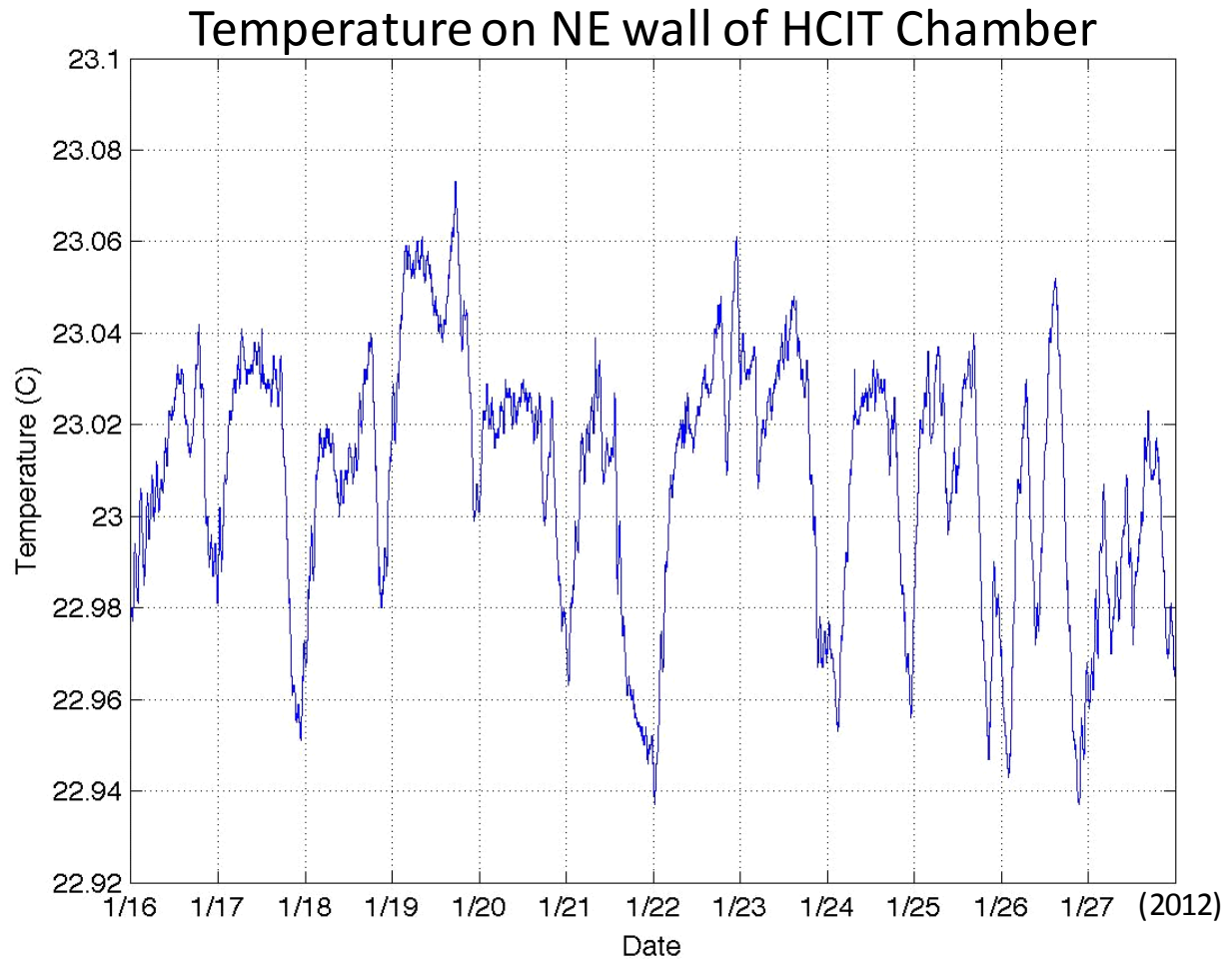
However, the system at hand also allows us to block the Lyot stop main opening and independently let light through the pinholes, one at a time or in pairs. These measurements can be used to better calibrate the model of the electric field due to the light going through the pinholes. The 10 intensity measurements are given by:

$$\begin{aligned}
 I_a &= |E_a|^2 \\
 I_b &= |E_b|^2 \\
 I_c &= |E_c|^2 \\
 I_d &= |E_d|^2 \\
 I_{ab} &= |E_a + E_b|^2 \\
 I_{ac} &= |E_a + E_c|^2 \\
 I_{ad} &= |E_a + E_d|^2 \\
 I_{bc} &= |E_b + E_c|^2 \\
 I_{bd} &= |E_b + E_d|^2 \\
 I_{cd} &= |E_c + E_d|^2
 \end{aligned} \tag{A3}$$

Using least squares minimization of the difference between the measured intensity and the model for it at each pixel, we find the complex electric field due to each of the pinholes per pixel in the image plane. This calibrated estimate is then used again to get a better estimate of  $E_0$  applying equation A2.

## APPENDIX II. THERMAL DATA

This plot shows the measured temperature from a sensor placed on the wall of the NE side of the vacuum chamber. This is the sensor closest to the Deformable Mirror. At the time of our experiments, there were no temperature sensors on the optical bench. The plot covers all the dates of our experiments. Note however that dates are UT.

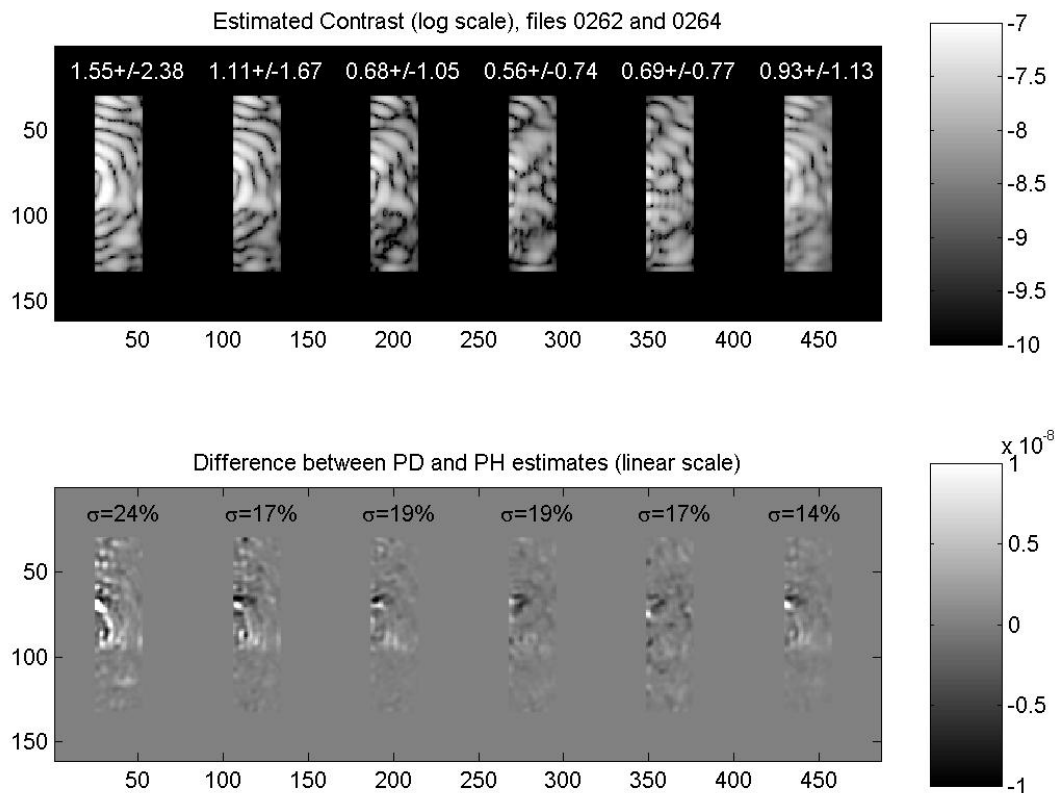


### APPENDIX III. ESTIMATED CONTRAST AND PHASE

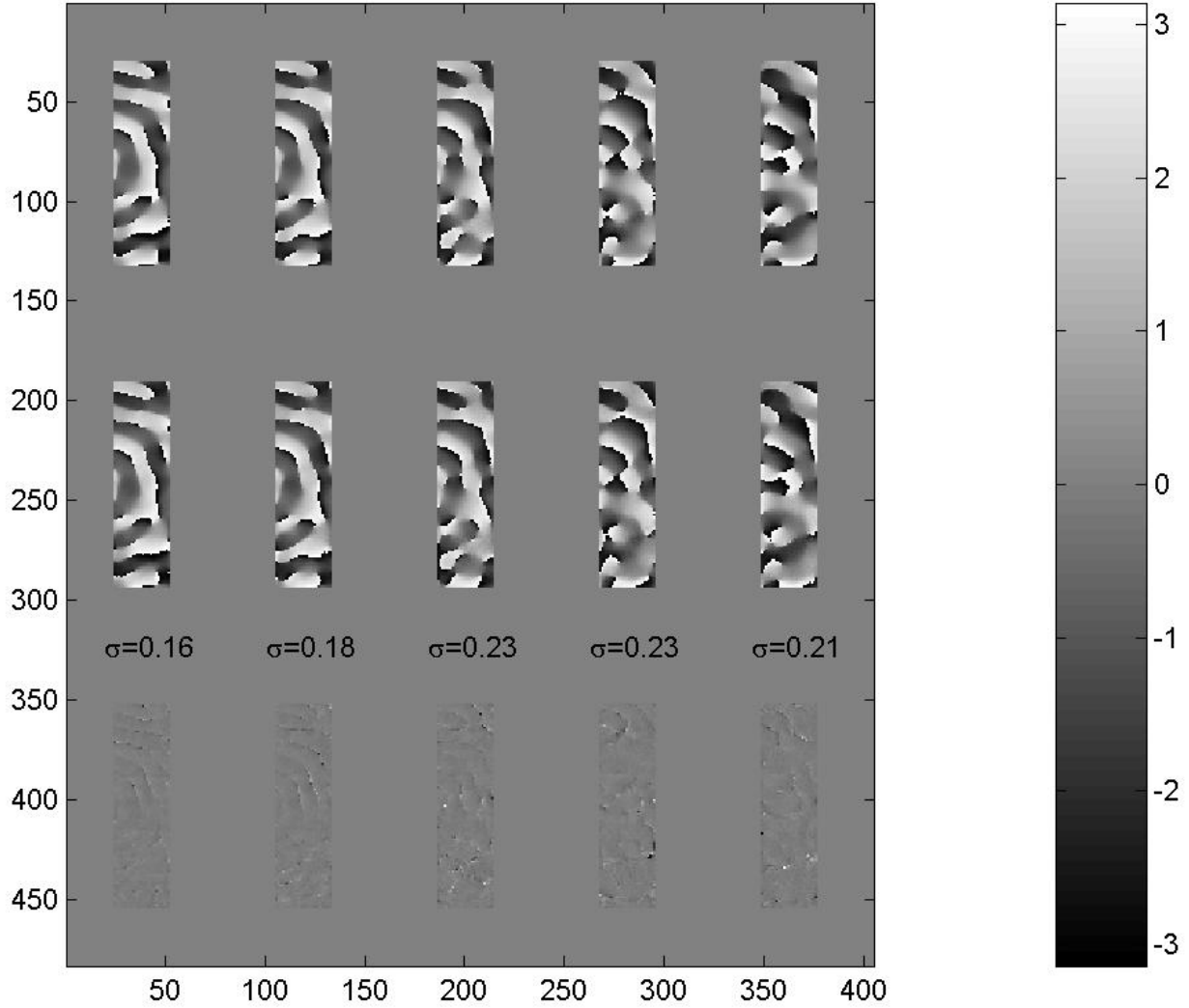
Contrast plots: Each contrast figure contains two images. The upper image is the estimated contrast based on Phase Diversity estimation. Six rectangular dark hole regions are plotted. From left to right, they are the signals through our 2% bandpass filters centered at 768, 784, 800, 816, and 832 nm. The rightmost dark hole is the composite broad band image formed from the average of the 5 bands. The grayscale on the right indicates contrast. The values plotted above each dark hole are the mean and standard deviation of contrast within the dark hole in each filter.

The bottom image shows the difference in estimated contrast between the PH and PD measurements. The value above each dark hole is the standard deviation of the difference between the PH and PD estimates.

Phase plots: Phase is calculated in the 5 bands. Plots are in radians. (There is no broadband phase map.) The upper set of dark hole regions contains the PD phase estimates in the five filters just described. The middle set contains the PH estimates. The lower set is the phase difference. The numbers above the phase difference plots are the standard deviation of the phase difference at each band.

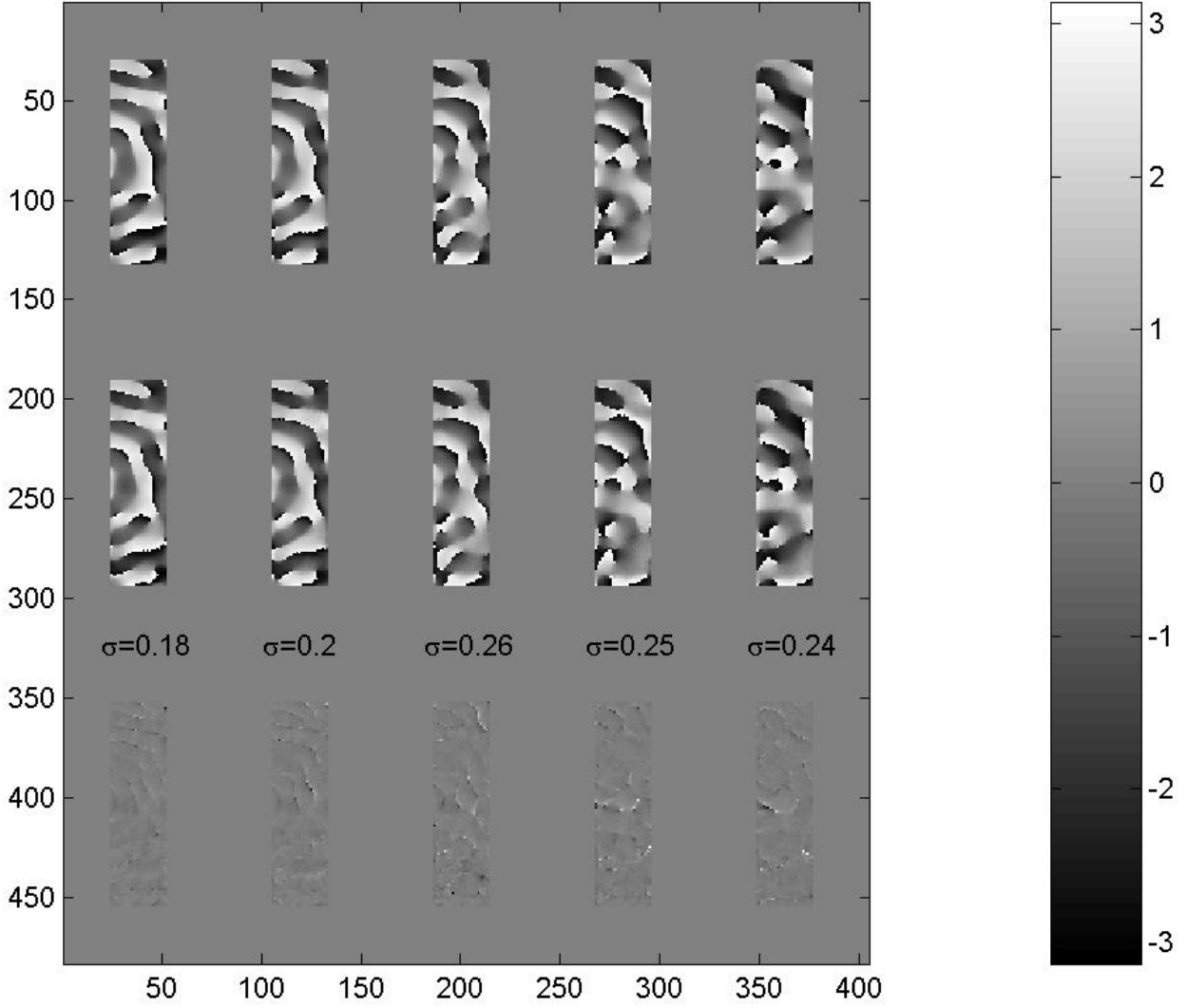


Run 1 Estimated dphase (radians), files 0262 and 0264

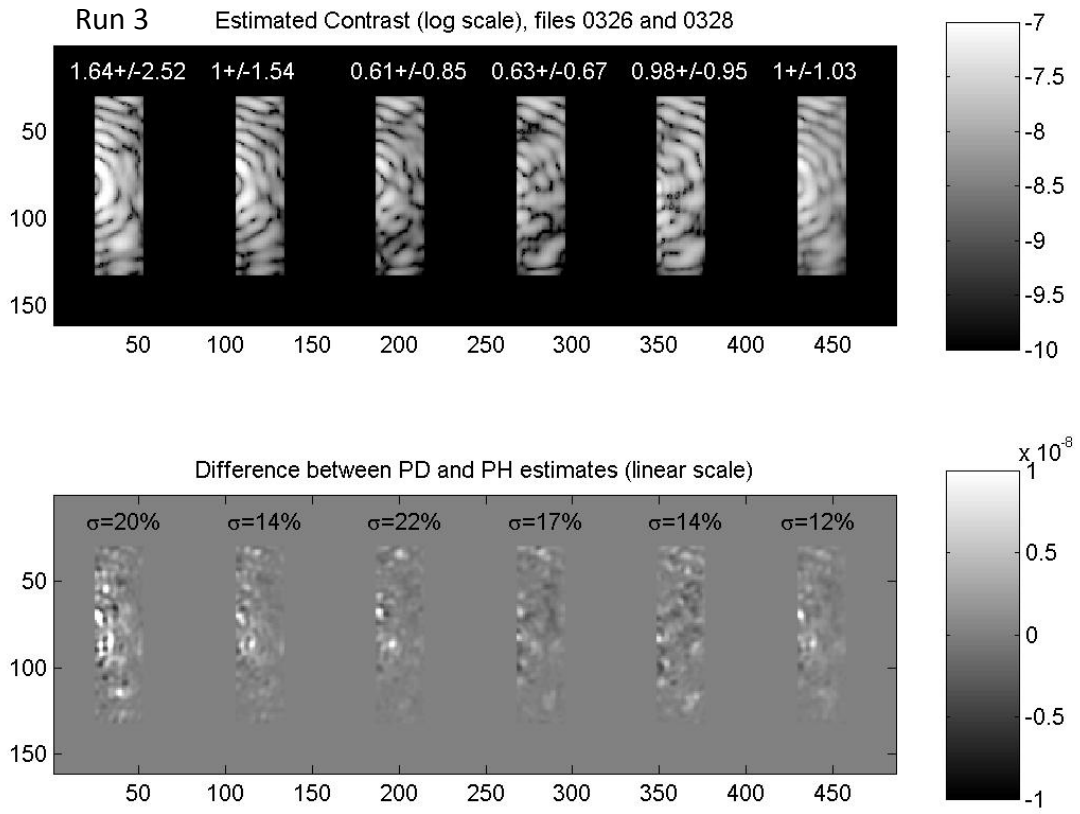




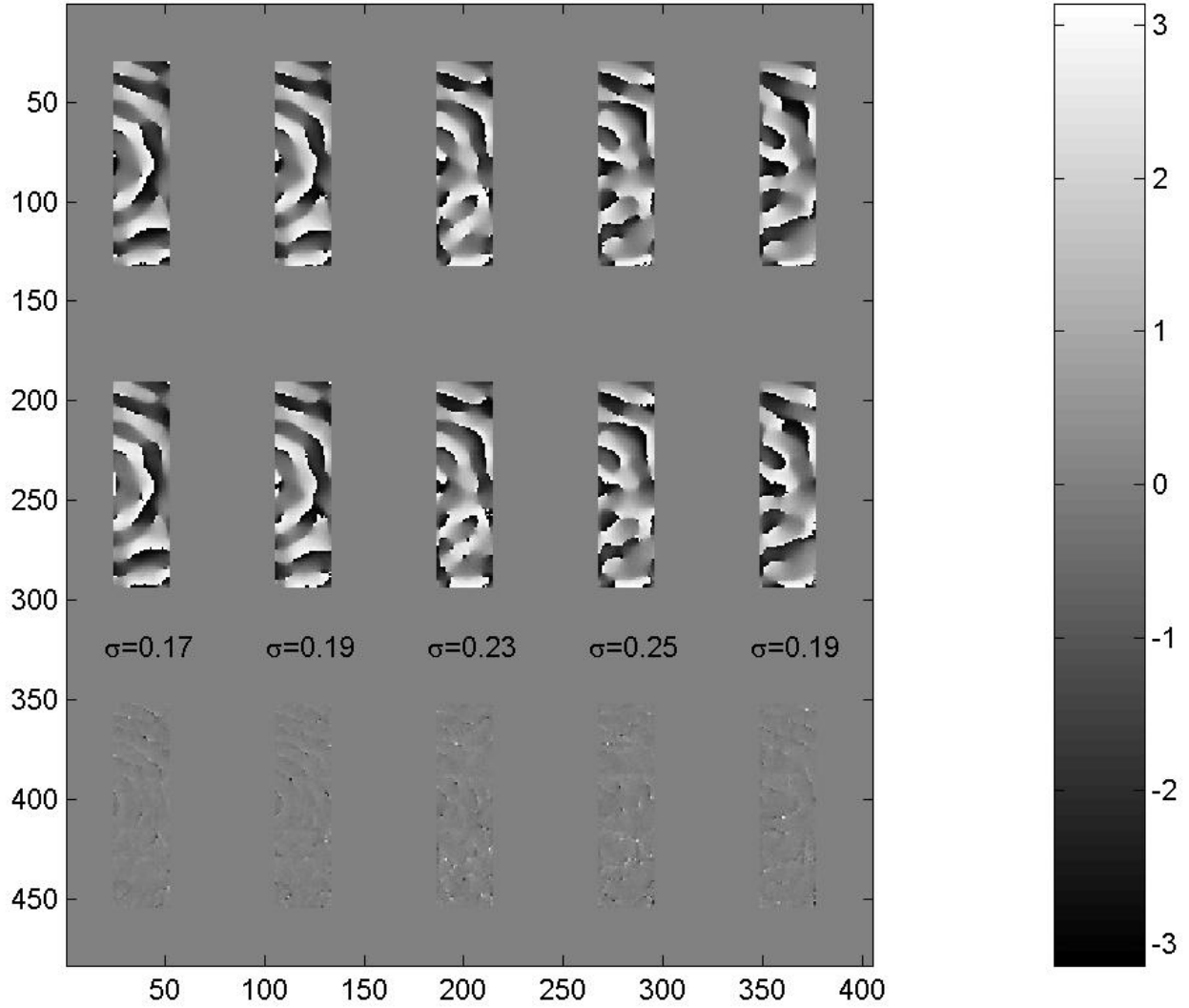
Run 2 Estimated dphase (radians), files 0290 and 0292



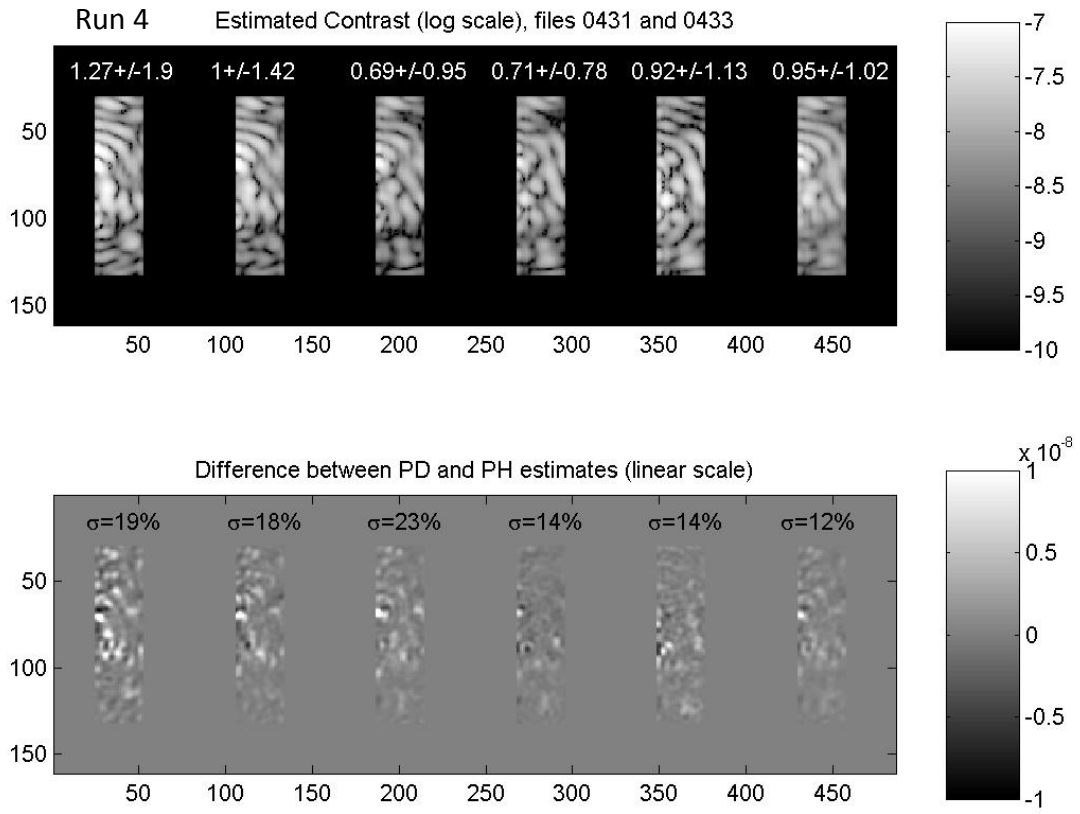
Technology Milestone Whitepaper  
Advanced Speckle Sensing for Internal Coronagraphs – Shaklan



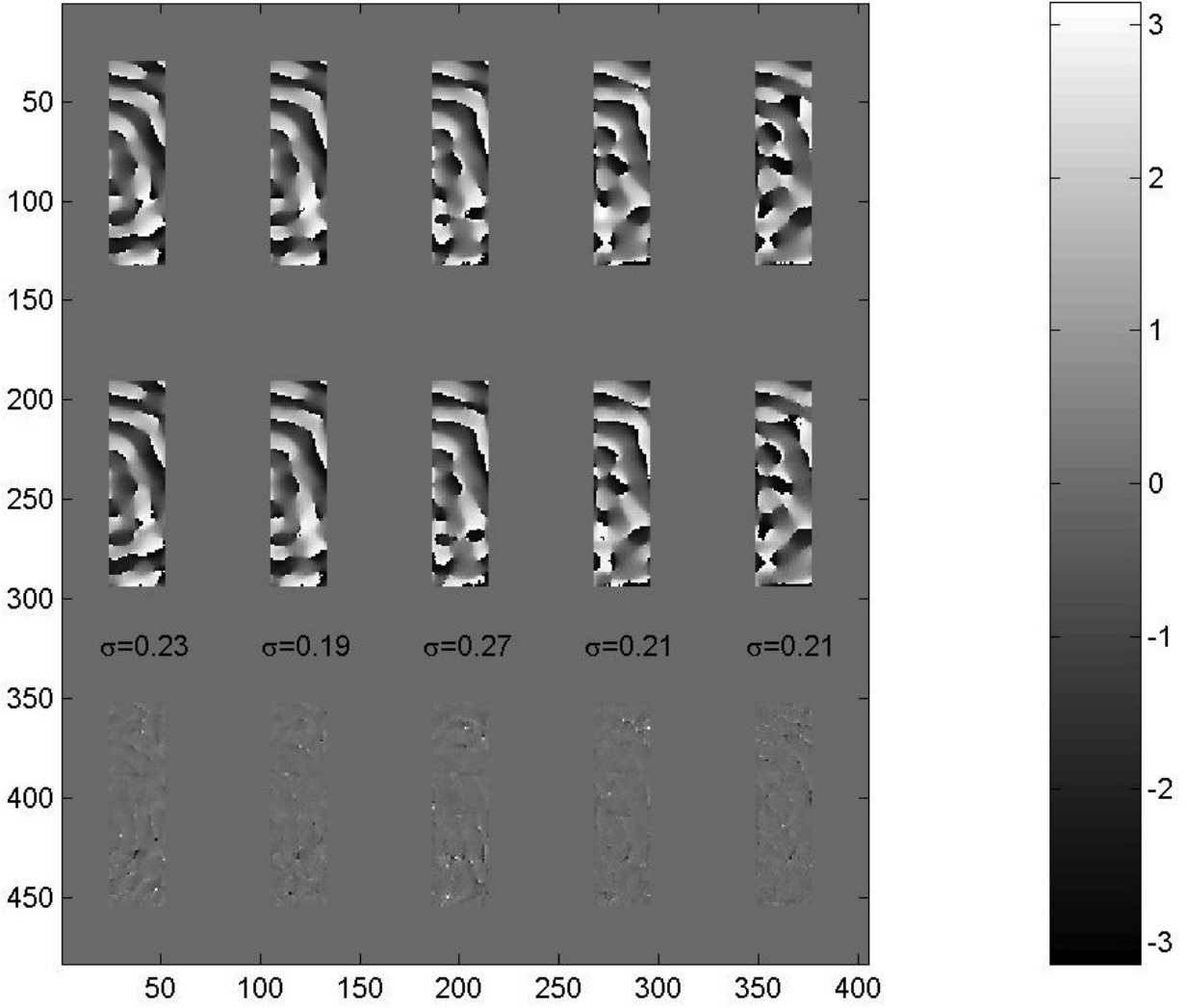
Run 3 Estimated dphase (radians), files 0326 and 0328



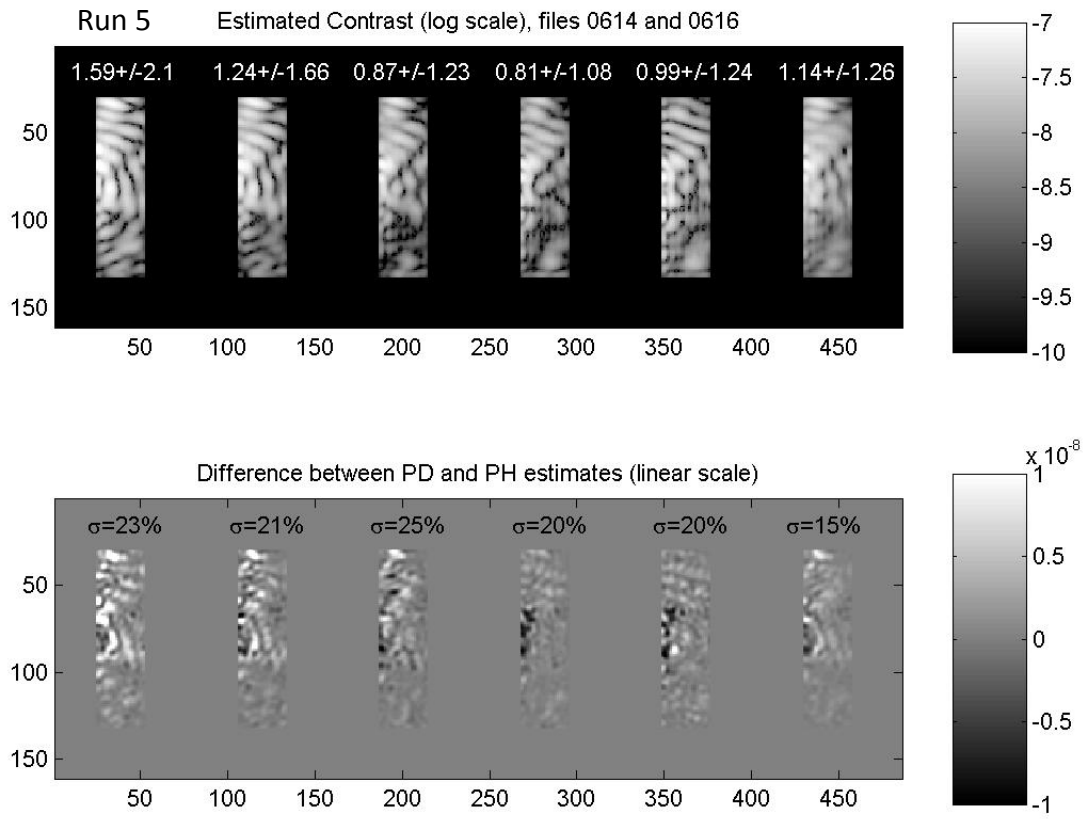
Technology Milestone Whitepaper  
Advanced Speckle Sensing for Internal Coronagraphs – Shaklan



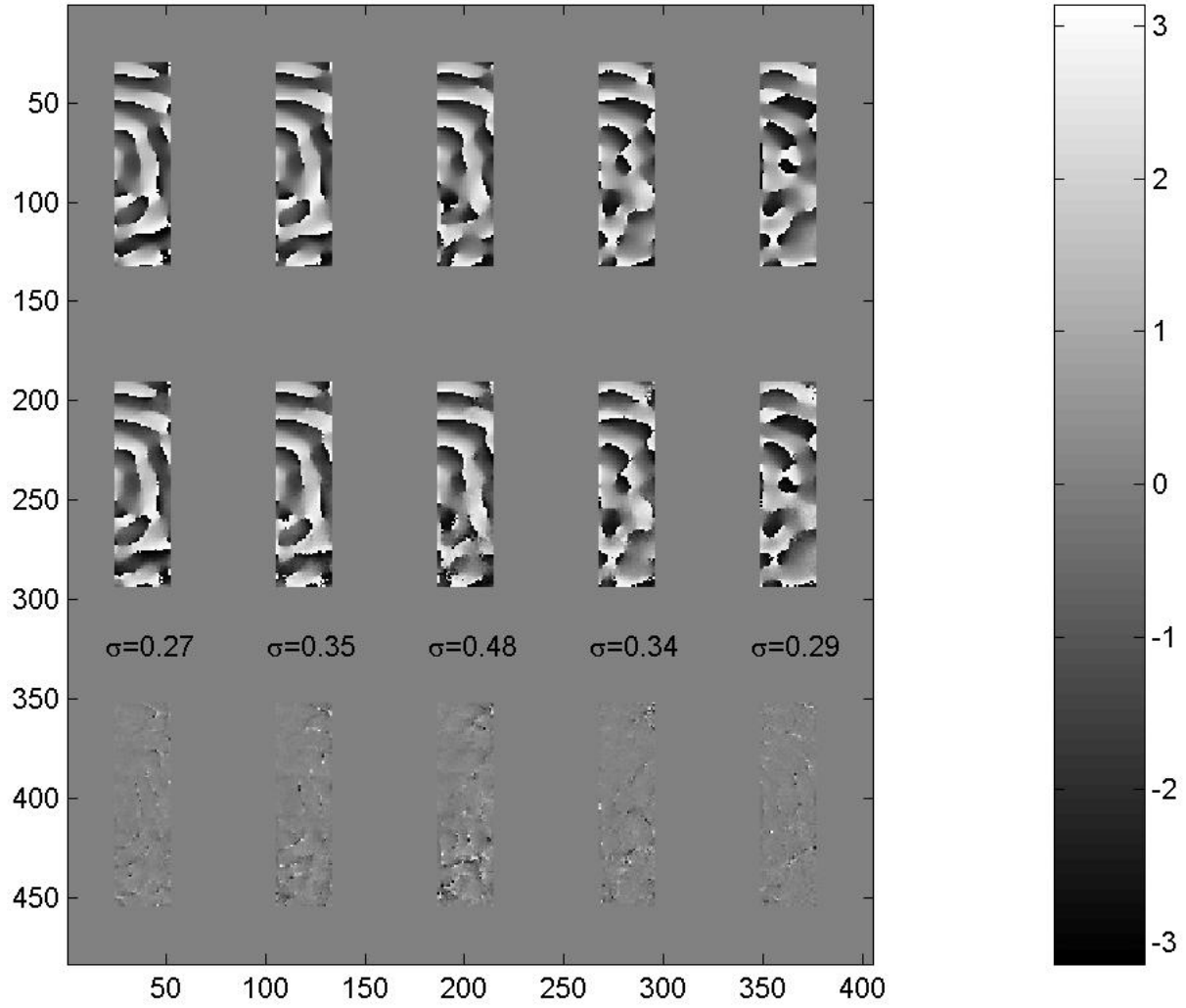
Run 4 Estimated dphase (radians), files 0431 and 0433



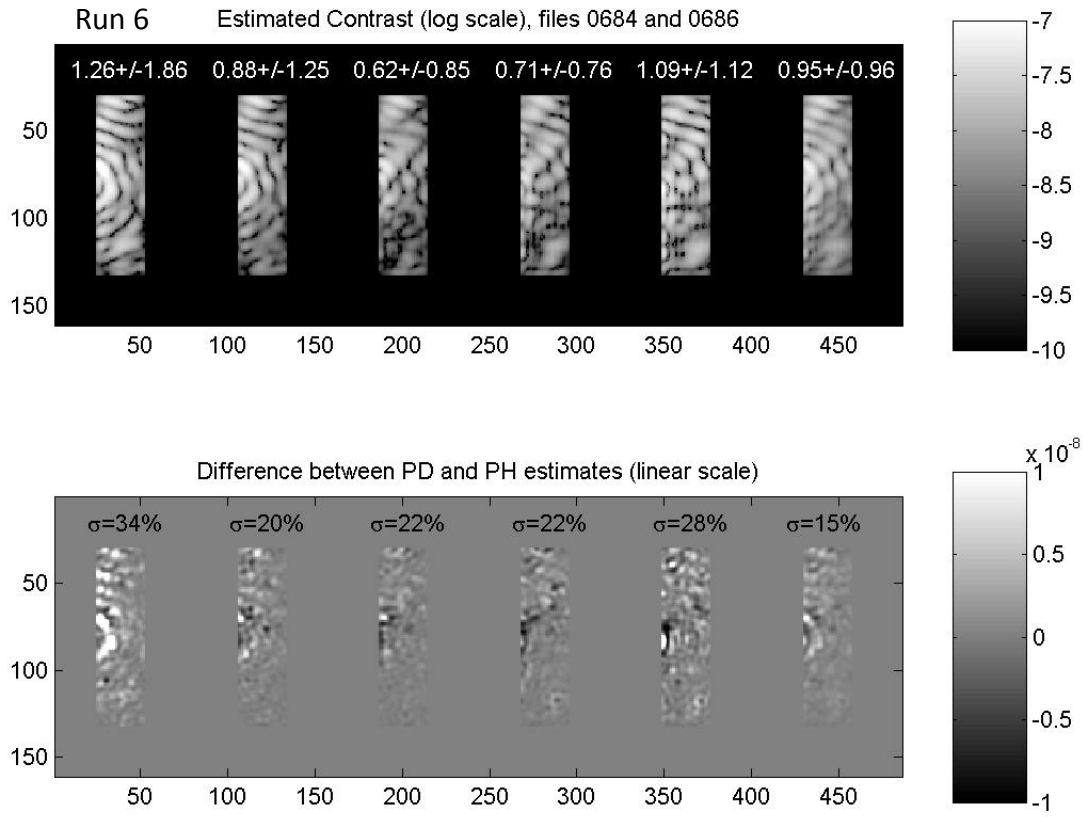
Technology Milestone Whitepaper  
Advanced Speckle Sensing for Internal Coronagraphs – Shaklan



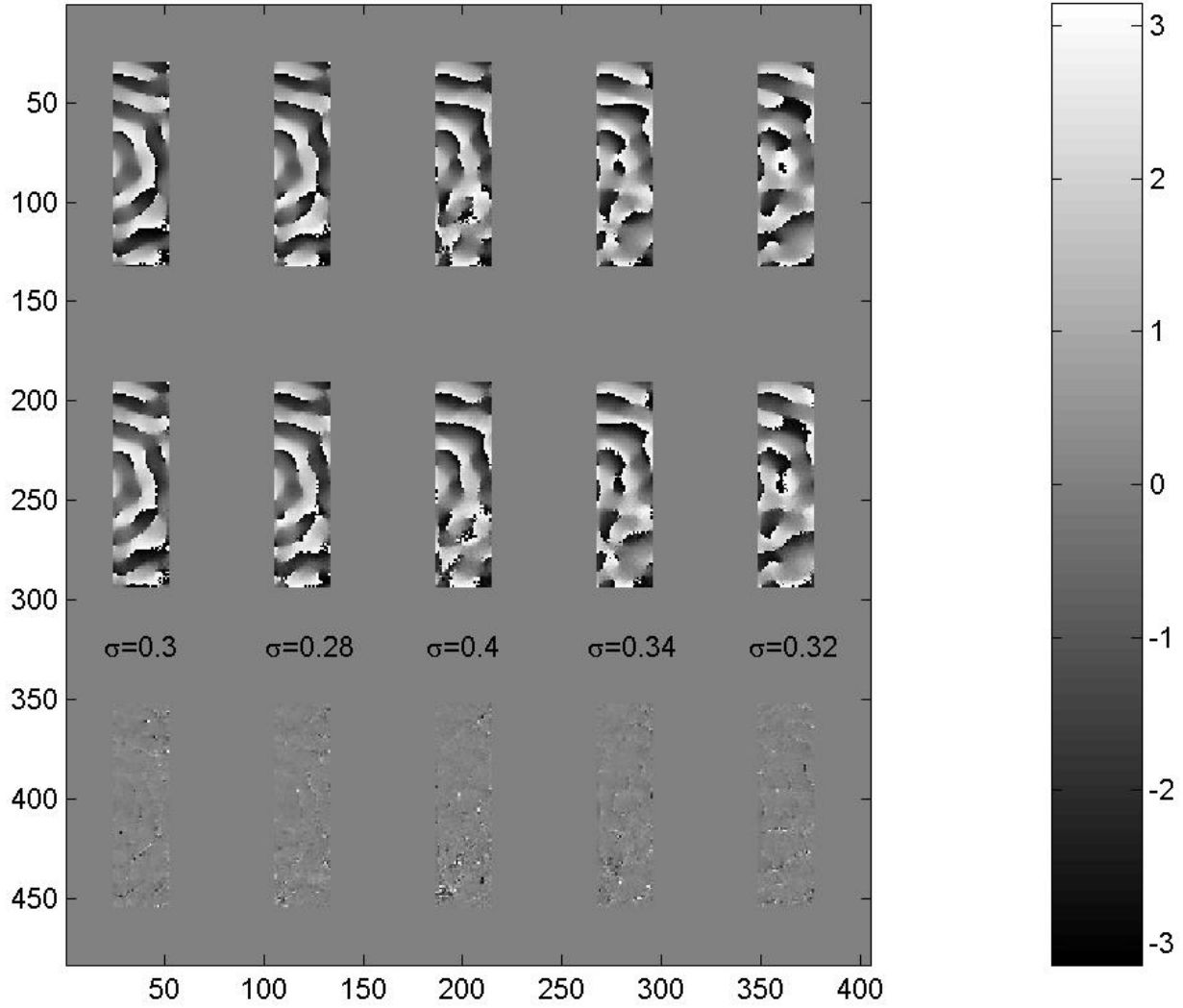
Run 5 Estimated dphase (radians), files 0614 and 0616



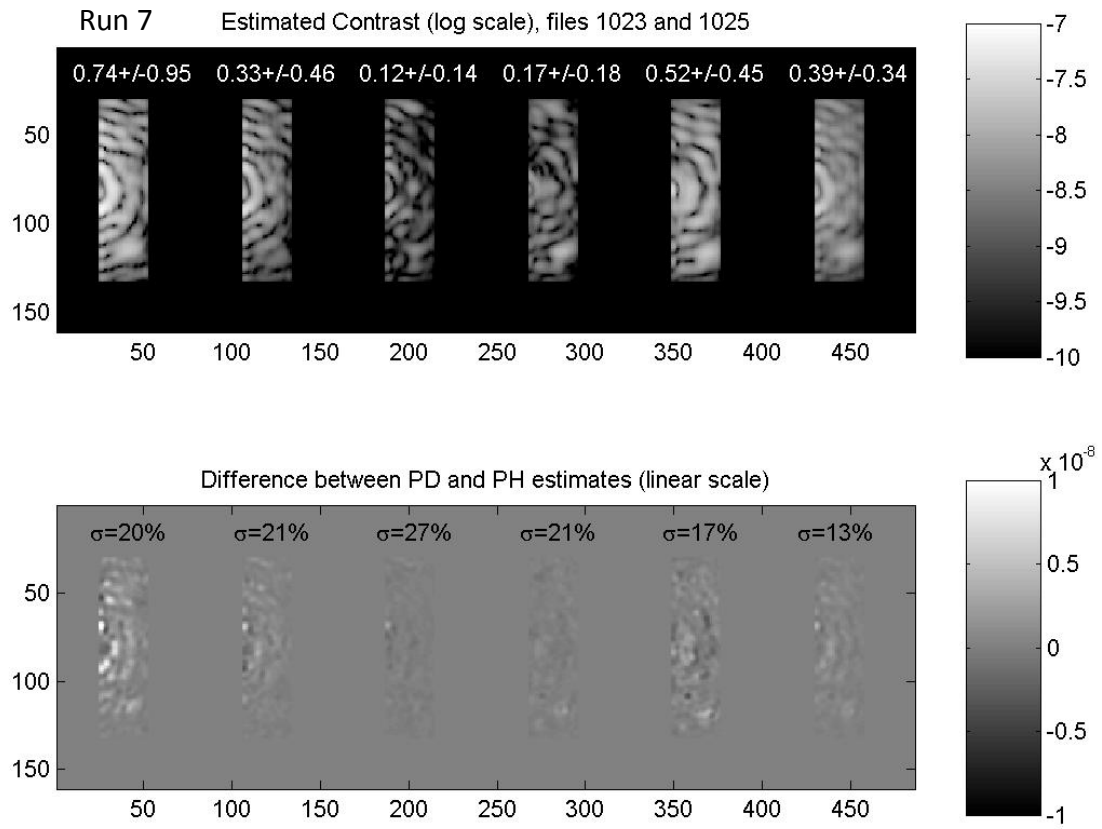
Technology Milestone Whitepaper  
Advanced Speckle Sensing for Internal Coronagraphs – Shaklan



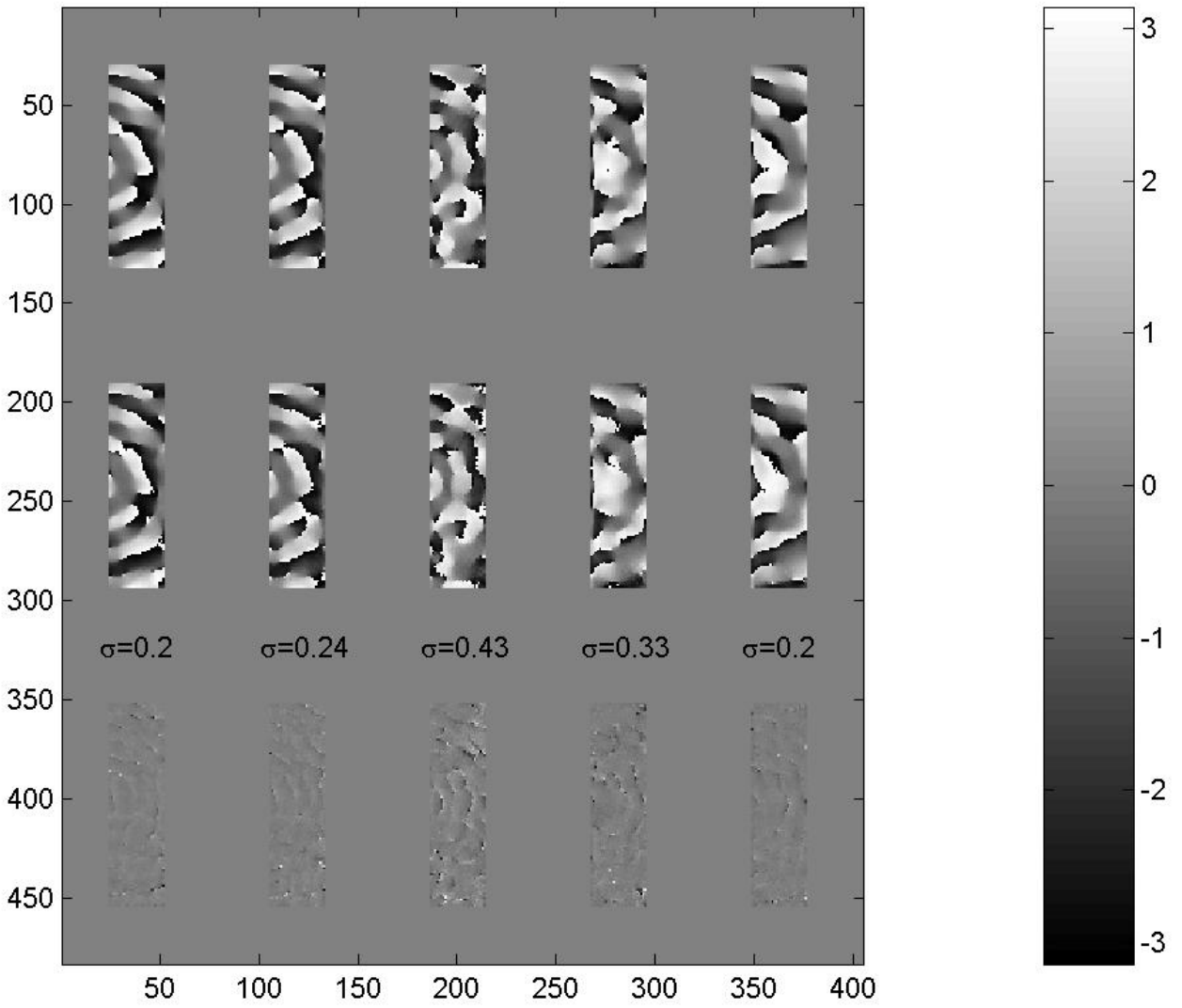
Run 6 Estimated dphase (radians), files 0684 and 0686



Technology Milestone Whitepaper  
Advanced Speckle Sensing for Internal Coronagraphs – Shaklan

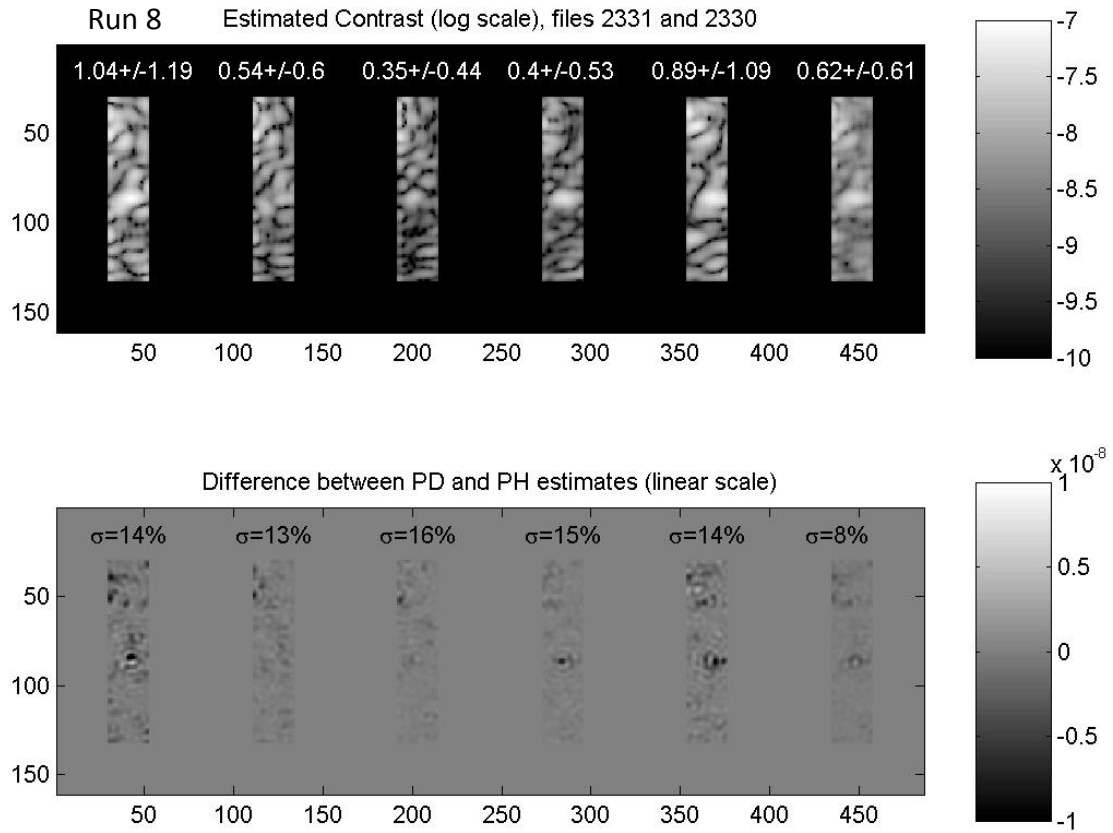


Run 7 Estimated dphase (radians), files 1023 and 1025



Technology Milestone Whitepaper  
Advanced Speckle Sensing for Internal Coronagraphs – Shaklan

This run shows the comparison of PD estimation with and without background lights turned on. Pinholes are not used here. The top row is the PD estimates without lights on. The bottom row shows the difference between lights-on/lights-off. Several weeks and several minor testbed modifications took place between run 7 and run 8. The mask position had been changed, and had a significant contaminant near the inner edge at  $4 \lambda/D$ . We avoided this region and analyze the region  $(5, 9) \lambda/D$  in  $x$  and  $(-9, +9) \lambda/D$  in  $y$ .



Technology Milestone Whitepaper  
Advanced Speckle Sensing for Internal Coronagraphs – Shaklan

Run 8 Estimated dphase (radians), files 2331 and 2330

